

# Computational studies of coarsening rates for the Cahn-Hilliard equation with phase-dependent diffusion mobility

Shibin Dai

*Department of Mathematical Sciences, New Mexico State University, Las Cruces, NM 88003, USA (sdai@nmsu.edu).*

Qiang Du

*Department of Applied Physics and Applied Mathematics, Columbia University, New York, NY 10027, USA (qd2125@columbia.edu).*

---

## Abstract

We study computationally coarsening rates of the Cahn-Hilliard equation with a smooth double-well potential, and with phase-dependent diffusion mobilities. The latter is a feature of many materials systems and makes accurate numerical simulations challenging. Our numerical simulations confirm earlier theoretical predictions on the coarsening dynamics based on asymptotic analysis. We demonstrate that the numerical solutions are consistent with the physical Gibbs-Thomson effect, even if the mobility is degenerate in one or both phases. For the two-sided degenerate mobility, we report computational results showing that the coarsening rate is on the order of  $l \sim ct^{1/4}$ , independent of the volume fraction of each phase. For the one-sided degenerate mobility, that is non-degenerate in the positive phase but degenerate in the negative phase, we illustrate that the coarsening rate depends on the volume fraction of the positive phase. For large positive volume fractions, the coarsening rate is on the order of  $l \sim ct^{1/3}$  and for small positive volume fractions, the coarsening rate becomes  $l \sim ct^{1/4}$ .

*Keywords:* Cahn-Hilliard equation, degenerate diffusion mobility, coarsening, power law

---

## 1. Introduction

Coarsening is a widely observed phenomenon in materials systems involving microstructures. It is characterized by the dissipation of excessive interfacial energy and the growth of a characteristic length scale. For instance, in alloys microstructures consist of precipitate particles of a minor phase embedded in a matrix of the major phase, and the characteristic length scale can be described by the diameter of the precipitate particles. Since the physical properties of

alloys are determined by the microstructures and the properties of the major and minor phases, the coarsening process has a dramatic effect on the properties of alloys.

In nickel-based superalloys, the diffusional mobility of the precipitate particles is between one and two orders of magnitude smaller than that of the Ni-matrix [2, 49]. This high disparity in diffusion mobility poses an interesting challenge in the modeling and analysis of the coarsening dynamics.

Mathematically speaking, coarsening phenomena are often characterized by a spatio-temporal power law, in which a characteristic length scale  $l(t)$  grows like a power of time. We write  $l \sim ct^{1/\alpha}$  to indicate such a power law, which means

$$l(t)^\alpha - l(t_0)^\alpha = c(t - t_0) \quad (1.1)$$

for some positive constant  $c$ . The exact value of the power  $\alpha$  depends on the coarsening mechanism for specific systems and has been actively explored theoretically and experimentally since the seminal LSW mean field theory for coarsening in dilute systems [31, 48]. The LSW theory predicts that the size distribution of the minor phase approaches a universal self-similar form, with the power  $\alpha = 3$ .

The LSW theory is the dilute limit of the Mullins-Sekerka model, in which coarsening is mediated by diffusion in bulk phases, see the review paper [47] for heuristic justifications and [33] for rigorous mathematical analysis. One key feature of the Mullins-Sekerka model is that the diffusion mobility is the same in both phases. Scaling argument suggests that the Mullins-Sekerka model follows a coarsening rate with a power  $\alpha = 3$ , see, e.g., [38].

Back to the case when the diffusivity is much smaller in the precipitate phase, it was proposed in [2] that coarsening in Ni-Al alloys is controlled by diffusion along the precipitate-matrix interface, and the coarsening rate corresponds to  $\alpha = 2$ , or  $\langle R \rangle \sim t^{1/2}$ , where  $\langle R \rangle$  is the average radius of the precipitate particles. However, it was acknowledged in [2] that a cubic root relation  $\langle R \rangle \sim t^{1/3}$  better fits experimental data. In [41], the coarsening in Ni-Al-Cr alloys was studied using atom-probe tomography (APT) and data fitting gives a relation  $\langle R \rangle \sim t^{0.30 \pm 0.04}$ . The coarsening in Ni-Al-Mo alloys was studied experimentally in [10] and numerically in [49] using phase-field simulations. Both experimental and numerical data can be fitted by a relation  $\langle R \rangle \sim t^{1/3}$ . It is thus reasonable to conclude that, when the diffusivity in the matrix of major phase is much bigger than that in the precipitate minor phase, we should still expect a coarsening rate with power  $\alpha = 3$ . The question is, what the coarsening mechanism is and what roles the disparity in diffusion mobility plays.

A first attempt to understand the effect of disparate diffusion mobility was carried out numerically in [43] in the framework of the Cahn-Hilliard (CH) equation, with a diffusion mobility that is constant in one phase and disappears in the second phase. Nonlinear data fitting in [43] shows a coarsening rate corresponding to a power  $\alpha \approx 3.3$ . This unusual rate motivated us to theoretically study the CH equation with a one-sided degenerate diffusion mobility using

asymptotic analysis [11]. We found that, due to the Gibbs–Thomson effect, there is a nontrivial porous-medium diffusion process in the phase where the diffusion mobility is degenerate and the coarsening mechanism depends on the volume fraction of the degenerate phase. In the case when the degenerate phase occupies a small fraction of the system, as in Ni-based alloys, coarsening is mediated through the diffusion process in the major non-degenerate phase, which can be interpreted as a one-sided Mullins–Sekerka model. Hence the coarsening rate has a power  $\alpha = 3$ . If, on the other hand, the degenerate phase occupies the majority of the system and the non-degenerate phase is of a small fraction, then it is the porous medium diffusion process in the degenerate phase that controls the coarsening process, and the coarsening rate has a power  $\alpha = 4$ .

A related problem is when the diffusion mobility is degenerate in both phases and non-degenerate in the interface separating the two phases [28, 29, 30]. It was conceived that the CH equation with a two-sided degenerate diffusion mobility models surface diffusion [28, 6, 45]. However, if the interface consists of disjoint pieces far away from each other, then surface diffusion does not provide communication between disjoint pieces and hence is not enough for coarsening to occur. Our study in [12] shows that, in this case it is the porous medium diffusion process in the degenerate bulk phases, together with surface diffusion, that mediates the coarsening process. The coarsening rate has a power  $\alpha = 4$ .

Our estimates of coarsening rates in [11, 12] are derived purely based on asymptotic analysis. It is natural to seek for further justifications through comparisons with experimental data and numerical simulations. The purpose of this paper is to present computational studies of the CH equations with phase-dependent diffusion mobilities that provide overwhelming support to our earlier theoretical findings. In Section 2 and 3, we describe Cahn–Hilliard equations and summarize the theoretically predicted coarsening mechanisms and rates for three cases of phase-dependent diffusion mobilities, along with the numerical scheme we use. Fourier spectral spatial discretizations of phase field models are known to offer superior accuracy even when examining the sharp interface limit [53]. We thus adopt such methods for the spatial discretization and combine it with a simple first order semi-implicit in time scheme. In Section 4 we present numerical results about the equilibration process of an ellipse into a circle, and show the difference due to the difference in the diffusion mobility, and the similarity of their final equilibrium state. In Sections 5 and 6 we report the numerical results for the cases with two-sided and one-sided degenerate diffusion mobility, respectively, with emphasis on the coarsening mechanisms and rates. Even though there have been numerous computational simulations for CH equations in the literature [3, 4, 5, 7, 8, 14, 16, 17, 18, 19, 20, 21, 23, 24, 25, 27, 32, 39, 40, 42, 43, 44, 46, 50, 51, 54, 55] and the references cited therein, the results given in this work represent the most comprehensive so far: we take small time steps in our simulations not only to ensure stability but most importantly to ascertain time accuracy; we run the simulations for exceedingly long time intervals so that the solution behaviors reach well into appropriate asymptotic regimes; we conduct numerical studies of a test case involving only an elliptical domain and another test case involving only two spherical domains

to demonstrate the consistency of numerical solutions with the physical Gibbs-Thomson effect and to illustrate the communication between disjoint domains and the mechanism behind the coarsening; we also carefully perform large scale simulations on systems involving convoluted spatial patterns to demonstrate the dependence of coarsening rates on the diffusion mobilities and volume fractions. For each case of two-sided and one-sided degenerate mobilities, we analyze three typical scenarios of 75%, 50% and 25% volume fractions corresponding to having large, equal and small positive phases and compare their coarsening rates. Together, these results enable us to make convincing justifications of our theoretical predictions on the coarsening rates and coarsening mechanisms. Finally in Section 7 we conclude our study with further discussions on related issues. In particular, we present some interesting observations on pre-asymptotic regimes and point out issues for future studies.

## 2. Cahn-Hilliard equations and their coarsening mechanisms

The CH equation is a phenomenological diffuse-interface model for a binary system. It is written as

$$u_t = \nabla \cdot \left( M(u) \nabla \left( -\varepsilon^2 \Delta u + F'(u) \right) \right) \quad \text{for } x \in \Omega \subset \mathbb{R}^n, t \in [0, \infty). \quad (2.1)$$

Here  $n \geq 2$  is the space dimension,  $M(u) \geq 0$  is the diffusion mobility and it depends on  $u$ , which is the relative concentration of the two phases.  $F(u)$  is a double-well potential with two equal minima at  $u^\pm$ , corresponding to the two phases. The CH equation is usually coupled with periodic or no-flux boundary conditions. During the evolution, the volume of each phase is preserved, and the interfacial energy

$$E(u) := \int_{\Omega} \left( \frac{\varepsilon^2}{2} |\nabla u|^2 + F(u) \right) dx \quad (2.2)$$

is decreasing. In this paper we will concentrate on a smooth double well potential with the often used quartic polynomial form

$$F(u) = \frac{1}{4}(u^2 - 1)^2, \quad (2.3)$$

whose minimizers are  $u^\pm = \pm 1$ .

For systems governed by the Cahn-Hilliard equation (2.1), the coarsening mechanism and rate (the power law) depend on the choice of the diffusion mobility  $M(u)$ .

### 2.1. $M(u) = 1$

When  $M(u)$  is a constant independent of  $u$ , the interface motion occurs in the  $t = O(\varepsilon^{-1})$  time scale and is described by the Mullins-Sekerka model [1, 9, 37]. Let  $\Gamma$  be the interface defined as the zero level curve of  $u$ , and  $\Omega_\pm$  be the regions

separated by  $\Gamma$  and occupied respectively by the positive and negative phases. In  $\Omega_{\pm}$  we formally expand  $u$  in powers of  $\varepsilon$  as  $u = \pm 1 + \varepsilon u_1 + O(\varepsilon^2)$ . Then the chemical potential  $\mu := -\varepsilon^2 \Delta u + F'(u)$  has a corresponding expansion  $\mu = \mu_0 + \varepsilon \mu_1 + O(\varepsilon^2)$  with  $\mu_0 = 0$  and  $\mu_1 = F''(\pm 1)u_1$ . Assume that  $\Gamma$  is sufficiently smooth and take  $\mathbf{n}$  as the unit normal to  $\Gamma$  pointing toward  $\Omega_+$ . Let  $V_{\mathbf{n}1}$  be the normal velocity of  $\Gamma$  in the rescaled time variable  $t_1 = \varepsilon t$ . The Mullins-Sekerka model says that the interface motion is determined by the following free boundary problem

$$\Delta \mu_1 = 0 \quad \text{in } \Omega_{\pm}, \quad (2.4)$$

$$\mu_1 = -S\kappa_0 \quad \text{on } \Gamma, \quad (2.5)$$

$$V_{\mathbf{n}1} = -\frac{1}{2}[\partial_{\mathbf{n}}\mu_1]_-^+ \quad \text{on } \Gamma. \quad (2.6)$$

Here  $\kappa_0$  is the mean curvature of  $\Gamma$ , defined by the sum of principal curvatures, and  $S$  is a positive constant determined by the double well potential  $F$ . The jump of flux across  $\Gamma$  is

$$[\partial_{\mathbf{n}}\mu_1]_-^+ := \partial_{\mathbf{n}}\mu_1^+ - \partial_{\mathbf{n}}\mu_1^- = \lim_{h \rightarrow 0^+} \mathbf{n} \cdot (\nabla \mu_1(x + h\mathbf{n}) - \nabla \mu_1(x - h\mathbf{n}))$$

for  $x \in \Gamma$ . For our choice of  $F$  in (2.3), the transition profile  $U(z) = \tanh(z/\sqrt{2})$  and

$$S = \frac{1}{2} \int_{-\infty}^{\infty} U'(z)^2 dz \approx 0.471. \quad (2.7)$$

So the interface motion is determined by a diffusion field in both phases, and the coarsening rate is a  $l \sim ct_1^{1/3} = c\varepsilon^{1/3}t^{1/3}$  power law in the intermediate  $O(\varepsilon^{-1})$  time scale, and for generic initial values. The interfacial area decreases according to

$$\frac{d|\Gamma|}{dt} = \varepsilon \frac{d|\Gamma|}{dt_1} = -\frac{\varepsilon}{2S} \int_{\Omega_+ \cup \Omega_-} |\nabla \mu_1|^2 dx \leq 0. \quad (2.8)$$

An immediate consequence of (2.8) is that an equilibrium state corresponds to  $\mu_1 = \text{constant}$  in both  $\Omega_+$  and  $\Omega_-$ . Due to (2.5), this requires  $\Gamma$  to have constant mean curvature. In 2D, this means that  $\Gamma$  has to be either straight lines or a circle, (or a collection of disjoint circles with the same radius, which is an unstable equilibrium state). When the equilibrium state consists of just one circle of radius  $r$ , if the interior of the circle consists of the positive phase, then  $\kappa_0 = -1/r$  and  $\mu_1 = S/r$ . If the interior of the circle consists of negative phase, then  $\kappa_0 = 1/r$  and  $\mu_1 = -S/r$ . Translating into  $u$ , we have

$$\begin{aligned} u &= \pm 1 + \frac{\varepsilon}{F''(\pm 1)} \mu_1 + O(\varepsilon^2) \\ &= \begin{cases} \pm 1 + \frac{\varepsilon S}{2r} + O(\varepsilon^2) & \text{in } \Omega_{\pm} \text{ if the interior of the circle is positive phase,} \\ \pm 1 - \frac{\varepsilon S}{2r} + O(\varepsilon^2) & \text{in } \Omega_{\pm} \text{ if the interior of the circle is negative phase.} \end{cases} \end{aligned} \quad (2.9)$$

The deviation from the *pure phases*  $\pm 1$ , which correspond to the two minimizers of the double-well potential  $F$ , of the amount  $\varepsilon S/(2r)$  is a consequence of the mathematical curvature effect (2.5), and corresponds to the physical Gibbs–Thomson effect, which says that pure phases can only exist when they are separated by flat interfaces. Inside small droplets of high curvature, due to excessive surface tension, the concentration is higher than that of the corresponding pure phases.

## 2.2. $M(u) = |1 - u^2|$

When  $M(u)$  is degenerate in both phases, in [12] we used asymptotic analysis to show that, as opposed to the intuition that the interface motion is purely determined by surface diffusion [6, 45], which does not allow coarsening if the interface consists of disjoint components, the actual interface motion is in fact determined by the combination of surface diffusion and a porous medium diffusion process in both phases, the latter provides communication between disjoint pieces of the interface. The nontrivial dynamics occurs in the  $t = O(\varepsilon^{-2})$  time scale. Let  $V_{\mathbf{n}2}$  be the normal velocity of  $\Gamma$  in the redefined time variable  $t_2 = \varepsilon^2 t$ , then it is determined by the following free boundary problem

$$\nabla \cdot (|\mu_1| \nabla \mu_1) = 0 \quad \text{in } \Omega_{\pm}, \quad (2.10)$$

$$\mu_1 = -S\kappa_0 \quad \text{on } \Gamma, \quad (2.11)$$

$$V_{\mathbf{n}2} = \sigma \Delta_s \kappa_0 - \frac{1}{2} \left[ |\mu_1| \partial_{\mathbf{n}} \mu_1 \right]_-^+ \quad \text{on } \Gamma. \quad (2.12)$$

Here  $\sigma$  is a positive constant determined by the double well potential  $F$ , and  $\Delta_s$  denotes the surface Laplacian on  $\Gamma$ . The jump of flux across  $\Gamma$  is  $\left[ |\mu_1| \partial_{\mathbf{n}} \mu_1 \right]_-^+ := |\mu_1^+| \partial_{\mathbf{n}} \mu_1^+ - |\mu_1^-| \partial_{\mathbf{n}} \mu_1^-$ , where

$$|\mu_1^{\pm}| \partial_{\mathbf{n}} \mu_1^{\pm}(x) := \lim_{h \rightarrow 0^+} |\mu_1(x \pm h\mathbf{n})| \mathbf{n} \cdot \nabla \mu_1(x \pm h\mathbf{n})$$

for  $x \in \Gamma$ . Scaling argument indicates that the coarsening rate is  $l \sim ct_2^{1/4} = c\varepsilon^{1/2}t^{1/4}$ . The interfacial area decreases according to

$$\frac{d|\Gamma|}{dt} = \varepsilon^2 \frac{d|\Gamma|}{dt_2} = -\varepsilon^2 \sigma \int_{\Gamma} |\nabla_s \kappa_0|^2 ds - \frac{\varepsilon^2}{2S} \int_{\Omega_+ \cup \Omega_-} |\mu_1| \cdot |\nabla \mu_1|^2 dx \leq 0. \quad (2.13)$$

The first term on the right hand side of (2.13) is the dissipation of interfacial area caused by surface diffusion. When  $\Gamma$  consists of disjoint pieces, surface diffusion equilibrates when each piece has constant curvature. The second term of (2.13) is dissipation caused by the porous medium diffusion process in  $\Omega_{\pm}$  (2.10)–(2.11). This porous medium diffusion process provides communication between disjoint pieces of  $\Gamma$ . In 2D, the equilibrium states of (2.10)–(2.12) correspond to  $\Gamma$  being either straight lines, or a circle, (or some disjoint circles of the same radius, which is unstable). In the case when the equilibrium state consists of just one circle, the equilibrium state is the same as (2.9).

Due to the degeneracy of the diffusion mobility  $M(u)$  in the two pure phases  $u^\pm = \pm 1$ , it has been conceived that if the initial value of  $u$  is inside  $[-1, 1]$ , then the solution  $u$  remains confined in  $[-1, 1]$  for all time [6, 45]. Indeed it was proved in [15] (and in [52] for the 1D case) that there exists such a  $u$ , confined in  $[-1, 1]$  for all time, as a solution for the Cahn-Hilliard equation in a weak sense. Apparently the weak solution studied in [15] will not be consistent with the curvature effect (2.11), or the physical Gibbs-Thomson effect. The existence of a solution, in a weak sense and different from the weak solution in [15], that is consistent with the Gibbs-Thomson effect, for the Cahn-Hilliard equation (2.1) with a two-sided degenerate mobility  $M(u) = |1 - u^2|$ , has recently been proved rigorously by the authors in [13].

### 2.3. $M(u) = \frac{1}{2}|1 + u|$

When  $M(u)$  is degenerate in one phase, the situation is more complicated. It was numerically investigated in [43] and a coarsening law of  $l \sim t^{1/3.3}$  was obtained using data fitting. This unusual rate motivated the analytical study in [11] using matched asymptotics. Translating into our setting here, the results in [11] show that (see Remark 1) for  $M(u) = \frac{1}{2}|1 + u|$ , there is a separation of time scales in the coarsening dynamics. In the  $t = O(\varepsilon^{-1})$  time scale, the interface motion is described by a one-sided Hele-Shaw problem

$$\Delta\mu_1 = 0 \quad \text{in } \Omega_+, \tag{2.14}$$

$$\mu_1 = -S\kappa_0 \quad \text{on } \Gamma, \tag{2.15}$$

$$V_{n1} = -\frac{1}{2}\partial_n\mu_1^+ \quad \text{on } \Gamma. \tag{2.16}$$

The interfacial area decreases according to

$$\frac{d|\Gamma|}{dt} = \varepsilon \frac{d|\Gamma|}{dt_1} = -\frac{\varepsilon}{2S} \int_{\Omega_+} |\nabla\mu_1|^2 dx \leq 0. \tag{2.17}$$

This is very similar to (2.8), except that here the integral is only over  $\Omega_+$ . Scaling argument implies that *if there is coarsening under the  $O(\varepsilon^{-1})$  dynamics (2.14)–(2.16)*, then the coarsening rate need to be  $l \sim ct_1^{1/3} = c\varepsilon^{1/3}t^{1/3}$ .

However, the one-sided feature of (2.14)–(2.16) indicates that, if there are disjoint components of  $\Omega_+$ , then these components will evolve independently without communication to each other, unless collision happens. If collisions do not occur, the *localized*  $t_1$ -dynamics drives each disjoint piece into spherical shapes and the localized  $t_1$ -dynamics equilibrates. A slower dynamics in  $t = O(\varepsilon^{-2})$  time scale kicks in, which is described by the following one-sided free boundary problem.

$$\nabla \cdot (|\mu_1|\nabla\mu_1) = 0 \quad \text{in } \Omega_-, \tag{2.18}$$

$$\mu_1 = -S\kappa_0, \quad \text{on } \Gamma, \tag{2.19}$$

$$V_{n2} = \frac{1}{8}|\mu_1|^- \partial_n\mu_1^- \quad \text{on } \Gamma. \tag{2.20}$$

The interfacial area decreases according to

$$\frac{d|\Gamma|}{dt} = \varepsilon^2 \frac{d|\Gamma|}{dt_2} = -\frac{\varepsilon^2}{8S} \int_{\Omega_-} |\mu_1| \cdot |\nabla \mu_1|^2 dx \leq 0. \quad (2.21)$$

The one-sided porous medium diffusion process (2.18) in  $\Omega_-$  provides communication between disjoint components of  $\Omega_+$  and coarsening is guaranteed. Scaling argument suggests a coarsening rate of  $l \sim ct_2^{1/4} = c\varepsilon^{1/2}t^{1/4}$ .

The separation of  $O(\varepsilon^{-1})$  and  $O(\varepsilon^{-2})$  dynamics depends on the volume fraction of the phases. Let  $\varphi$  be the volume fraction occupied by the positive phase. We consider three situations. When the positive phase occupies a large fraction of the system, that is,  $\varphi$  is near 1, the negative phase breaks into disjoint pieces and the coarsening is mediated through the diffusion field in the positive phase. When  $\varphi$  is about 0.5, both the positive and the negative phases are essentially connected. The porous medium diffusion process in the negative phase is one order in  $\varepsilon$  slower than the diffusion process in the positive phase. Hence the coarsening is again mediated through the diffusion field in the positive phase. In both cases the coarsening rate is  $l \sim ct_1^{1/3}$ . When the positive phase occupies a small fraction of the system, that is when  $\varphi$  is close to 0, the positive phase breaks into disjoint pieces and the coarsening process is mediated through the porous medium diffusion process in the negative phase, which is much slower and gives a coarsening rate  $l \sim ct_2^{1/4}$ .

As for the equilibrium state, (2.17) and (2.21) imply that, in 2D when the equilibrium configuration consists of just one circle, the equilibrium state is again (2.9).

**Remark 1.** *In [11] we chose a one-sided degenerate mobility  $M(u)=1+u$  and assumed the existence of a smooth solution. After we finished [11], further studies in [12, 13] and results in this work have indicated that, without absolute value on  $1+u$ , the choice of  $M(u) = 1 + u$  may not guarantee the existence of a smooth solution, unless the positive phase consists of disjoint convex regions. In addition, in [11] we expanded the principal curvatures of the interface in powers of  $\varepsilon$ . We think it makes the calculation unnecessarily complicated and we ditched such expansion of curvatures in [12] and this paper. Nevertheless, with minor modifications the results in [11] can be translated into the setting in this paper, resulting in (2.14)–(2.16) and (2.18)–(2.20).*

### 3. Numerical scheme and setup

We solve the Cahn-Hilliard equation (2.1) complemented with periodic boundary condition on a square domain using a semi-implicit spectral method as in [8, 43]. Let  $\mathcal{F}_k$  be the  $k_{\text{th}}$  mode of the Fourier transform and  $\mathcal{F}_k^{-1}$  the inverse Fourier transforms, respectively, that is, for any  $f \in L^1(\Omega)$ , denoting by  $\hat{f}$  the Fourier transform of  $f$ ,

$$\hat{f}(k) := \mathcal{F}_k(f(x)) = \int_{\Omega} f(x) e^{-ik \cdot x} dx, \quad (3.1)$$

$$f(x) = \mathcal{F}_k^{-1}(\hat{f}(k)) = \frac{1}{(2\pi)^n} \int_{\mathbb{R}^n} \hat{f}(k) e^{ik \cdot x} dk. \quad (3.2)$$

Let  $\mu := -\varepsilon^2 \Delta u + F'(u)$  be the chemical potential. Its Fourier transforms is  $\hat{\mu}(k, t) = \varepsilon^2 |k|^2 \hat{u}(k, t) + \mathcal{F}_k(F'(u))$ . The semi-implicit time discretization is to split the mobility  $M(u)$  into a positive constant  $M_0$  and  $M(u) - M_0$ , and then to treat the term involving  $M_0$  implicitly and the term involving  $M(u) - M_0$  explicitly. Equivalently, it is to introduce a splitting term  $-\varepsilon^2 M_0 \Delta^2 u(x, t^{n+1}) + \varepsilon^2 M_0 \Delta^2 u(x, t^n)$  to the equation and we get

$$\begin{aligned} & (1 + \Delta t \varepsilon^2 M_0 |k|^4) \hat{u}(k, t^{n+1}) \\ &= (1 + \Delta t \varepsilon^2 M_0 |k|^4) \hat{u}(k, t^n) + \Delta t i k \cdot \mathcal{F}_k \left( M(u(x, t^n)) \mathcal{F}_{k'}^{-1} \left( ik' \hat{\mu}(k', t^n) \right) \right). \end{aligned} \quad (3.3)$$

$M_0$  is chosen to be

$$M_0 = \frac{1}{2} \left( \max_{u \in (-1, 1)} \{M(u)\} + \min_{u \in (-1, 1)} \{M(u)\} \right).$$

For this work, we have  $M_0 = 1/2$ . We need to keep in mind that this choice of  $M_0$  is only intuitive, since due to curvature effects, the values of  $u$  are not necessarily confined in  $[-1, 1]$ . But since the deviation of  $u$  outside of  $[-1, 1]$  is of order  $O(\varepsilon)$ , in practice the choice  $M_0 = 1/2$  works fine numerically.

To calculate the coarsening rate, we use two methods. The first is the energy density. Since the Cahn-Hilliard energy (2.2) is proportional to the area of the interface  $\Gamma$  (more precisely, the  $\Gamma$ -limit of the rescaled Cahn-Hilliard energy  $\frac{1}{\varepsilon} E$  is the interface area, multiplied by a constant), the energy density  $\bar{E}(u) := E(u)/|\Omega|$  has a dimension of  $(\text{length})^{-1}$ . Consequently if the coarsening rate is  $l \sim ct^{1/\alpha}$ , we expect  $\bar{E}^{-\alpha}(u(t)) - \bar{E}(u(t_0))^{-\alpha} = C(t-t_0)$  for some constant  $C$ , or equivalently

$$\ln \bar{E}(u(t)) = -\frac{1}{\alpha} \ln t + C_1 + o(1) \quad (3.4)$$

when  $\bar{E}(u(t)) \ll \bar{E}(u_0)$ .

The second method to estimate the characteristic length is to use the correlation function. Define the spatial pointwise correlation function  $\tilde{G}(x, t)$  as

$$\tilde{G}(x, t) = \frac{1}{|\Omega|} \int_{\Omega} \left( u(x+x', t) u(x', t) - \bar{u}^2 \right) dx'. \quad (3.5)$$

The average correlation function  $G(r, t)$  and the normalized correlation function  $g(r, t)$  are

$$G(r, t) = \frac{1}{r} \int_{|x|=r} \tilde{G}(x, t) d\sigma(x), \quad \text{and} \quad g(r, t) = \frac{G(r, t)}{G(0, t)}.$$

The characteristic length is then defined as the first root  $R(t)$  of  $g(r, t)$ . If the coarsening rate is  $l \sim ct^{1/\alpha}$ , we expect  $R(t) \sim ct^{1/\alpha}$  or equivalently

$$\ln R(t) = \frac{1}{\alpha} \ln t + C_2 + o(1) \quad (3.6)$$

when  $R(t) \gg R(0)$ .

For our simulations, the domain is taken as a square  $\Omega = [0, k\pi]^2$  with an  $N \times N$  uniform grid. We choose  $N$  so that the grid size  $h = \frac{k\pi}{N} \leq \frac{1}{4}\varepsilon$  so we have reasonable resolution of the interface profile. The diffuse interfacial width parameter is set to a constant value  $\varepsilon = 0.05$ . As a consequence we choose  $N = 256k$  and the grid size is  $h \approx 0.01227$ . The values of  $k$  are 1, 2, 4 or 8, varying from section to section. These parameters have been tested to assure sufficient accuracy in all simulations.

It is worthwhile to point out that the asymptotic analysis in [11, 12, 37] works for any space dimension  $n \geq 2$ . The coarsening mechanisms and rates are independent of space dimension as long as  $n \geq 2$ . We thus expect to see similar results if one carries out careful and accurate large-scale simulations in 3D. The latter sure presents a formidable computational challenge, but we note that there has been much progress in recent years on algorithmic improvements (see, e.g., [7, 8, 17, 18, 19, 23, 24, 25, 42, 44, 46, 50, 51, 54, 55] and the references cited therein). Comparisons of these different schemes are also interesting exercises but are beyond the scope of this work. Here, we focus on numerical simulations in 2D for computational illustrations of the coarsening dynamics and leave more 3D benchmark studies and comparisons of different numerical algorithms to future explorations.

#### 4. The equilibration process and the equilibrium state

The first thing we study is the effect of the phase-dependent diffusion mobility on the equilibration process and the equilibrium state. We consider a system with a simple initial configuration of one ellipse. In this section, the domain is  $\Omega = [0, \pi]^2$  and  $N = 256$ .

There are two situations. The first is that the ellipse consists of the positive phase and the second is that the ellipse consists of the negative phase. We choose the center of the ellipse as  $(x_0, y_0) = (\frac{\pi}{2}, \frac{\pi}{2})$  and the semi-major and semi-minor axes as  $a = 0.3\pi, b = 0.2\pi$ . We place the ellipse so that its major axis lies along the diagonal  $\{y = x\}$  of the domain  $\Omega$ , which corresponds to  $\theta = \frac{\pi}{4}$ , where  $\theta$  is the angle between the major axis and the  $x$ -axis. The ellipse corresponds to the 1-level curve of

$$R(x, y) := \frac{((x - x_0) \cos \theta + (y - y_0) \sin \theta)^2}{a^2} + \frac{(-(x - x_0) \sin \theta + (y - y_0) \cos \theta)^2}{b^2}.$$

We define our initial value as

$$u_0(x, y) = 0.9 \tanh \frac{1 - R(x, y)}{\sqrt{2}\varepsilon}. \quad (4.1)$$

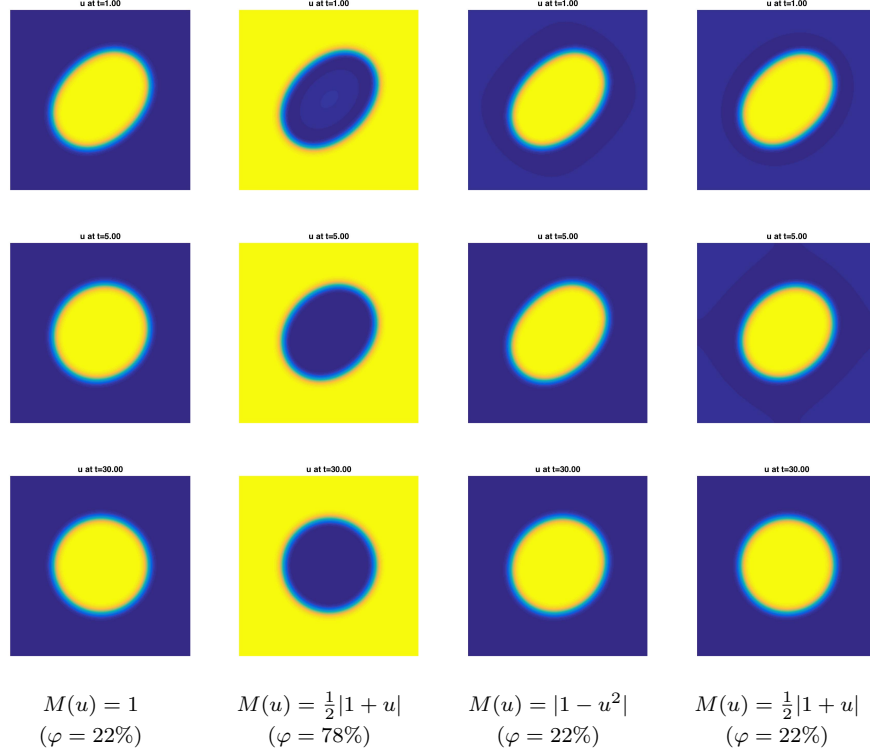


Figure 1: The equilibration process of an ellipse into a circle.  $\Omega = [0, \pi]^2, \varepsilon = 0.05, N = 256$ . Top row:  $t = 1$ ; Middle row:  $t = 5$ ; Bottom row:  $t = 30$ . (left column):  $M(u) = 1, \varphi = 22\%, \Delta t = 1 \times 10^{-4}$ ; (middle left column):  $M(u) = \frac{1}{2}|1+u|, \varphi = 78\%, \Delta t = 5 \times 10^{-6}$ ; (middle right column):  $M(u) = |1-u^2|, \varphi = 22\%, \Delta t = 1 \times 10^{-4}$ ; (right column):  $M(u) = \frac{1}{2}|1+u|, \varphi = 22\%, \Delta t = 2.5 \times 10^{-6}$ .

This gives an ellipse whose interior is the positive phase, and the positive phase occupies  $\varphi = 22\%$  of the system. To obtain an ellipse whose interior is the negative phase, we just take the initial value as  $-u_0$ , which gives  $\varphi = 78\%$ , see Fig. 1.

The equilibration is characterized by two features. The first is that the system converges into a clear separation of two phases,  $u \approx 1$  and  $u \approx -1$ , respectively, with a thin layer in between. The second is that the ellipse morphs into a circle, which corresponds to the minimization of the interface area between the two phases. Fig. 1 shows the transformation of the ellipse into a circle, for the three diffusion mobilities  $M(u) = 1, M(u) = \frac{1}{2}|1+u|$  and  $M(u) = |1-u^2|$ , and the two situations  $\varphi = 22\%$  and  $\varphi = 78\%$ . Note that since the initial values are  $u_0$  and  $-u_0$  defined by (4.1), and since the mobilities  $M(u) = 1, M(u) = |1-u^2|$  and the double well potential  $F(u)$  defined by (2.3) are even functions of  $u$ , for these two mobilities, the behaviors of the system for  $\varphi = 78\%$  are the same as that for  $\varphi = 22\%$ , as long as we interchange the positive and negative

phases. For the non-symmetric one-sided degenerate case of  $M(u) = \frac{1}{2}|1+u|$ , even though the second column ( $\varphi = 78\%$ ) of Fig. 1 appears to be very similar to the fourth column ( $\varphi = 22\%$ ) if we interchange the positive and negative phases, there is in fact a significant difference in the dynamics between  $\varphi = 22\%$  and  $\varphi = 78\%$ , as qualitatively described in Section 2.

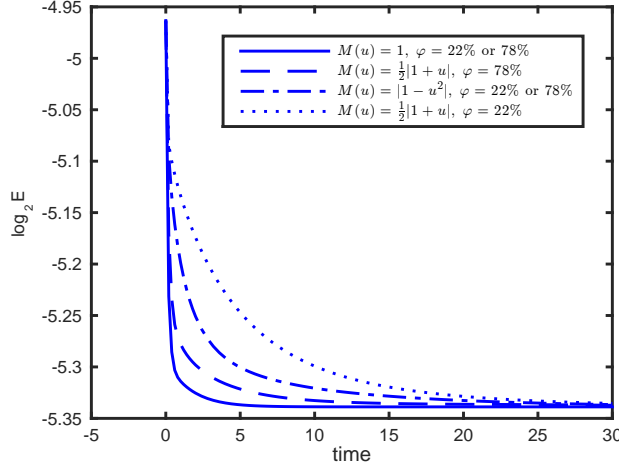
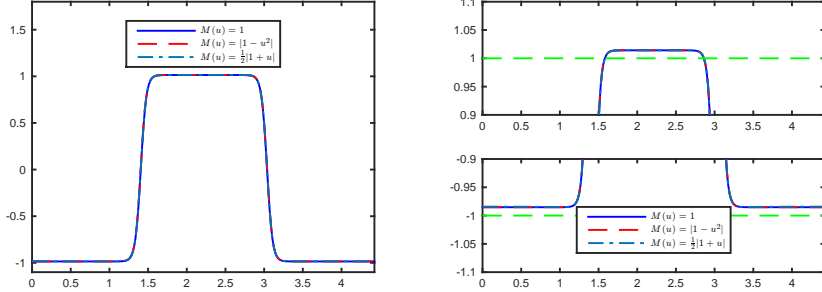
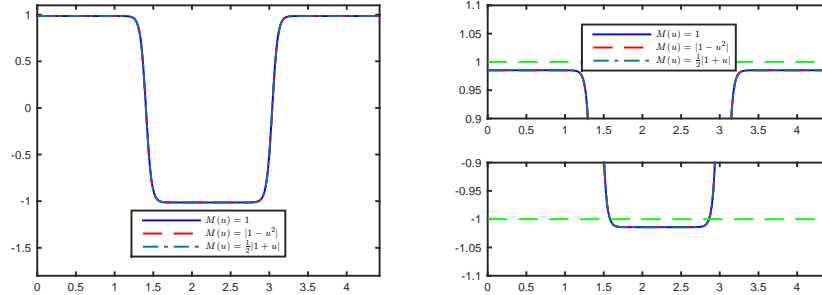


Figure 2: The dissipation of energy during the equilibration of an ellipse into a circle, depicted as  $\log_2 E(t)$  vs. time.

One way to study the equilibration process is to study the energy dissipation. Fig. 2 shows the semi-log plots of energy vs. time. The following is an explanation of the difference in the energy dissipation rates depicted in Fig. 2.

- (i) . (fastest)  $M(u) = 1$  with  $\varphi = 22\%$  or  $78\%$ . According to (2.8), interfacial area dissipation occurs in the  $O(\varepsilon^{-1})$  time scale, and is determined by the diffusion process in both  $\Omega_+$  and  $\Omega_-$ .
- (ii) . (second fastest)  $M(u) = \frac{1}{2}|1+u|$  with  $\varphi = 78\%$ . According to (2.17), interfacial area dissipation occurs in the  $O(\varepsilon^{-1})$  time scale, and is determined by the diffusion process in  $\Omega_+$  only. Hence it is conceivable that the dissipation is slower than that in case (i).
- (iii) . (slower)  $M(u) = |1-u^2|$  and  $\varphi = 22\%$  or  $78\%$ . According to (2.13), interfacial area dissipation occurs in the slower  $O(\varepsilon^{-2})$  time scale, which generically is slower than dissipations in the faster  $O(\varepsilon^{-1})$  time scale. The dissipation is determined by surface diffusion and porous medium diffusion process in both  $\Omega_+$  and  $\Omega_-$ .
- (iv) . (slowest)  $M(u) = \frac{1}{2}|1+u|$  with  $\varphi = 22\%$ . According to (2.21), interfacial area dissipation occurs in the slower  $O(\varepsilon^{-2})$  time scale, and is determined by the porous medium diffusion process in the negative phase. Hence it is conceivable to be slower than case (iii).

Figure 3: ( $\varphi = 22\%$ ) Vertical cross sections of  $u$  along the diagonal  $\{y = x\}$ , at time  $t = 100$ .Figure 4: ( $\varphi = 78\%$ ) Vertical cross sections of  $u$  along the diagonal  $\{y = x\}$ , at time  $t = 100$ .

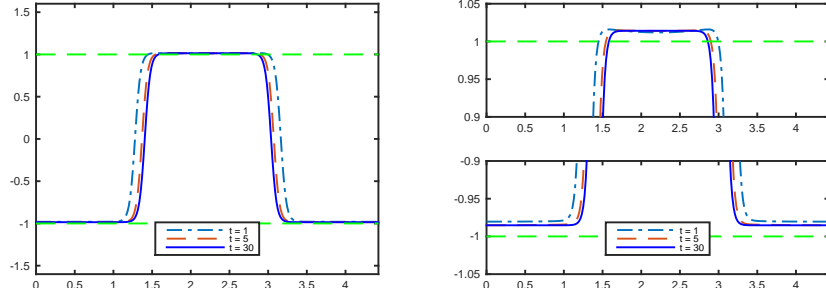
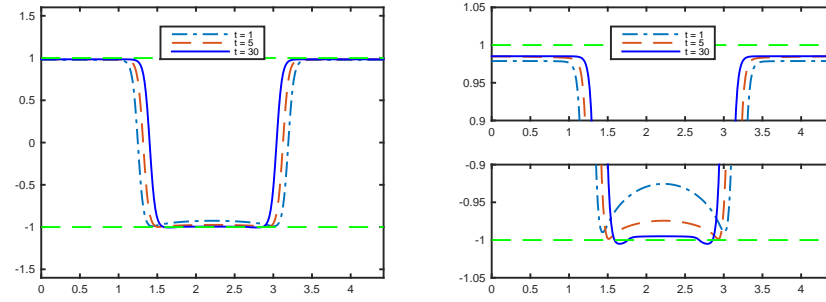
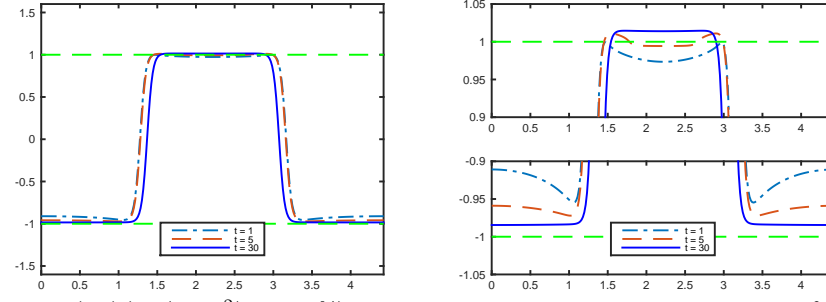
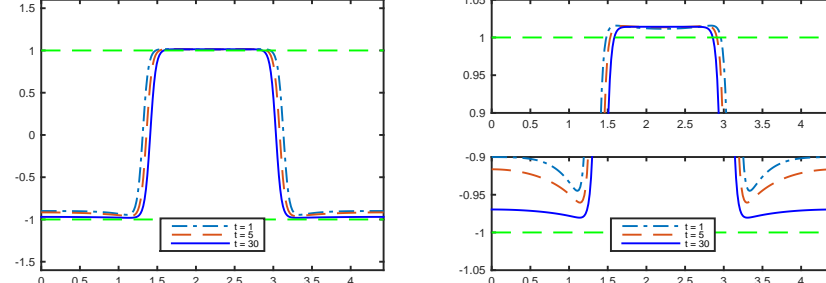
To numerically compare the equilibrium states of the system corresponding to different diffusion mobilities, we plot the vertical cross sections of  $u$  and their zooms around  $u \approx \pm 1$  along the diagonal  $\{y = x\}$  of the domain  $\Omega$ , at time  $t = 100$  for the three choices of  $M(u)$  and  $\varphi = 22\%$  in Fig. 3 and for  $\varphi = 78\%$  in Fig. 4. The differences in the profiles of  $u$  due to different  $M(u)$  are negligible. Hence this confirms our claim in Section 2 that, if the initial values are the same, then the system arrives at the same equilibrium state, even if we choose different phase-dependent diffusion mobilities. In addition, our simulations show that in both positive and negative phases, the equilibrium values of  $u$  have a deviation of the magnitude 0.014 from the *pure phases*  $\pm 1$ . This quantitatively agrees with our theoretical prediction of the Gibbs-Thomson effect in (2.9). Indeed, for  $\varphi = 22\%$ , since the domain is  $\Omega = [0, \pi]^2$ , in the leading order the equilibrium radius  $r$  of the positive phase should satisfy

$$\pi r^2 = 0.22\pi^2, \quad \text{or } r \approx 0.8313. \quad (4.2)$$

Then by (2.7), (2.9) and  $\varepsilon = 0.05$ , neglecting the  $O(\varepsilon^2)$  term, the deviation from  $\pm 1$  should be

$$\frac{\varepsilon S}{2r} \approx 0.014. \quad (4.3)$$

There are surely significant differences in the equilibration processes for different  $M(u)$ . Figs. 5–8 show the vertical cross sections of  $u$  at time  $t = 1, 5$  and

Figure 5:  $(M(u) = 1, \varphi = 22\%)$  Vertical cross sections of  $u$  along the diagonal  $\{y = x\}$ .Figure 6:  $(M(u) = \frac{1}{2}|1+u|, \varphi = 78\%)$  Vertical cross sections of  $u$  along the diagonal  $\{y = x\}$ .Figure 7:  $(M(u) = |1-u^2|, \varphi = 22\%)$  Vertical cross sections of  $u$  along the diagonal  $\{y = x\}$ .Figure 8:  $(M(u) = \frac{1}{2}|1+u|, \varphi = 22\%)$  Vertical cross sections of  $u$  along the diagonal  $\{y = x\}$ .

30.

- (i) . For  $M(u) = 1$  and  $\varphi = 22\%$ , we can see in Fig. 5 that for  $t = 5$  and  $t = 30$ , in the positive and negative phases, there is no visible difference for the values of  $u$ . There is visible, but very small, difference in the transition region. So it is conceivable that the system can be considered to have arrived at its equilibrium at  $t = 30$ , (although technically the system can only asymptotically approach its equilibrium, and never really *arrive at it*). This can also be justified by the fact that in the semi-log energy vs. time plot (Fig. 2),  $\log_2 E(t)$  is literally flat for  $10 < t < 30$ . Also the first column of Fig. 1 shows that at  $t = 30$ , the positive phase is enclosed by a perfect circle.
- (ii) . For  $M(u) = \frac{1}{2}|1 + u|$  and  $\varphi = 78\%$ , Fig. 6 shows that, even though in the positive phase the value of  $u$  already arrives at its equilibrium value at  $t = 30$ , its value in the negative phase (the interior of the circle) has not. The rest of the dynamics is to equilibrate  $u$  inside the circle. Since the interface between the two phases is already driven into a perfect circle (the second column of Fig. 1), and there is only a small deviation of  $u$  away from its eventual equilibrium value inside the negative phase, and the negative phase is only a small fraction of the system, the rest of the dynamics will cause a very minor decrease of energy, as evidenced by the very small negative slope of  $\log_2 E$  vs. time in Fig. 2.
- (iii) . For  $M(u) = |1 - u^2|$  and  $\varphi = 22\%$ , even though it is hard to tell from Fig. 7, it is clear from Fig. 1 that at  $t = 30$  the interface is not yet circular, hence  $u$  has not arrived at its equilibrium at  $t = 30$ . This can also be seen in Fig. 2, where  $\log_2 E$  vs. time has a non zero slope at  $t = 30$ .
- (iv) . For  $M(u) = \frac{1}{2}|1 + u|$  and  $\varphi = 22\%$ , although from the fourth column of Fig. 1 we see that the interface is already circular at  $t = 30$ , from Fig. 8 it is clear that  $u$  has not arrived at its equilibrium value in the negative phase, that is, the outside of the circle.

## 5. Simulations with a two-sided degenerate mobility $M(u) = |1 - u^2|$

### 5.1. Details of morphology

To further illustrate the details of morphological changes during the evolution, we do a numerical simulation of a system consisting of two circles that are far apart initially. During the evolution, they stayed far apart from each other.

The domain is  $\Omega = [0, A]^2$  with  $A = 2\pi$  and  $N = 512$ . The initial profile consists of two radially symmetric suppressed tanh profiles whose 0-level curves are the following two circles with radii  $r_i$  and centers  $X_i = (x_i, y_i)$ , ( $i = 1, 2$ ) on the diagonal  $\{(x, y) \in \Omega : x = y\}$  of  $\Omega$ :

$$x_1 = 0.7A, y_1 = 0.7A, r_1 = 0.1A; \quad x_2 = 0.3A, y_2 = 0.3A, r_2 = 0.2A.$$

The initial profiles are

$$\max \left\{ 0.9 \tanh \left( \frac{r_i - |X - X_i|}{\sqrt{2}\varepsilon} \right) : i = 1, 2 \right\} \quad (5.1)$$

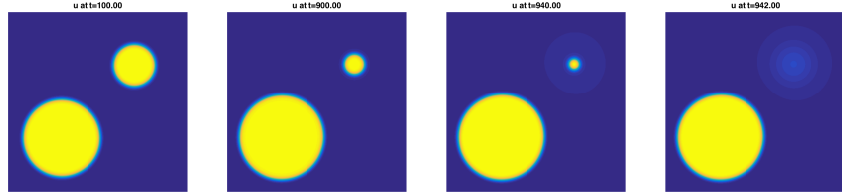


Figure 9: ( $M(u) = |1 - u^2|$ , two circles) Morphological patterns at  $t = 100$ ,  $t = 900$ ,  $t = 940$  and  $t = 942$  (from left to right). Coarsening is mediated through the porous medium diffusion fields in both phases, together with surface diffusion along the interface.  $\Omega = [0, 2\pi]^2$ ,  $\varepsilon = 0.05$ ,  $N = 512$ ,  $\Delta t = 5 \times 10^{-6}$  for  $0 < t \leq 52$  and  $\Delta t = 1 \times 10^{-4}$  for  $52 < t \leq 1000$ .

where  $X = (x, y)$  is any point in the domain. This simulation serves two purposes: first, we demonstrate that, as predicted by our asymptotic analysis theory, even if initial values are in  $(-1, 1)$ , under the influence of the curvature effect, in later time  $u$  goes bigger than 1 in the two circular positive phases, and  $u$  is bigger than  $-1$  in the negative phase. Secondly, while the bigger one grows, the smaller circle shrinks, slowly in a time scale proportional to  $\varepsilon^{-2}$ . This indicates that there is communication between the two disjoint circles, hence the evolution is not confined inside the transition region around the interface.

Fig. 9 shows typical morphologies of the system during coarsening. We can see that the two circular droplets of positive phase remain circular for all time, the big one grows while the small one shrinks, very slowly in a time scale proportional to  $\varepsilon^{-2}$ . When the time eventually comes for the small circle to collapse, it happens in a short period of time.

Since the boundary condition is periodic, we expect the dynamics to keep the symmetry with respect to the diagonal of  $\Omega$ . Hence the profile of  $u$  at each time can be characterized by the vertical cross sections of  $u$  along the diagonal of  $\Omega$ , see, Fig. 10 and 11. It can be seen from Fig. 10 that  $u$  is always bigger than  $-1$ . And from Fig. 11 it is clear that in a short time,  $u$  first becomes bigger than 1 inside the small circular region, and later it also becomes bigger than 1 inside the big circular region. This is because smaller circles have bigger curvatures and the curvature effect is stronger. Also, from the bottom figures of Fig. 11 we see that when the small circle shrinks, hence its curvature grows, the value of  $u$  inside it also grows. In contrast, while the big circle grows, its curvature decreases and the value of  $u$  inside it also decreases, but always bigger than 1. Such coarsening behavior agrees with that predicted by our sharp interface model (2.10)–(2.12).

To demonstrate the sufficiency of our spatial resolution, in Fig. 12 we show the profiles of  $u$  at  $t = 100$ , in the same domain  $\Omega = [0, 2\pi]^2$ , with the same initial value of two circles (5.1), and the same time step  $\Delta t = 1 \times 10^{-4}$ , but different spatial resolution  $N = 256, 512$  and  $1024$ . There is no visible difference. Hence it is fair to say that the consistency with the Gibbs–Thomson effect of our numerical simulations is not an artifact due to roundoff errors, but is indeed a genuine feature of the model, as theoretically predicted by our asymptotic

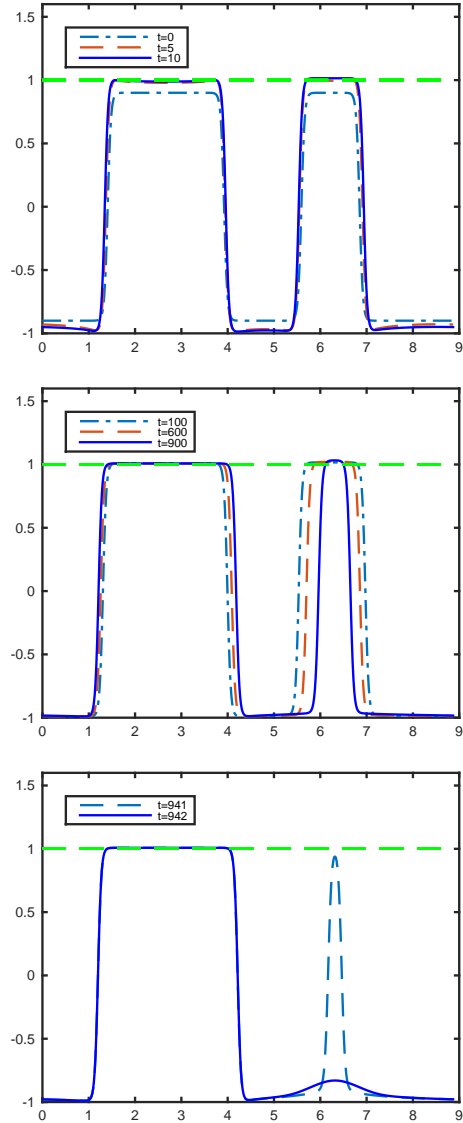


Figure 10: ( $M(u) = |1 - u^2|$ , two circles) Vertical cross sections of  $u$  along the diagonal direction  $y = x$  of the domain  $\Omega$ , at  $t = 0, 5, 10$  (top)  $t = 100, 600, 900$  (middle), and  $t = 941$  and  $942$  (bottom).

analysis in [12].

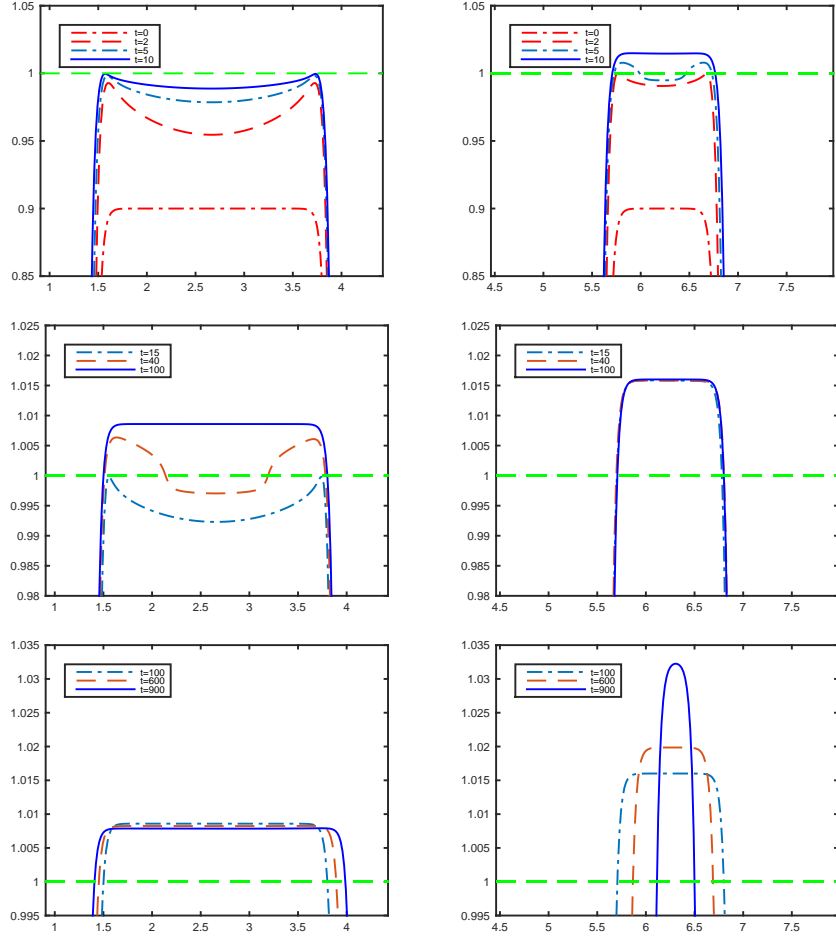


Figure 11:  $M(u) = |1 - u^2|$ , two circles) Zoom of the vertical cross sections of  $u$  along the diagonal direction  $y = x$  of the domain  $\Omega$ , at  $t = 0, 2, 5, 10$  (top)  $t = 15, 40, 100$  (middle), and  $t = 100, 600, 900$  (bottom). The left column is the big circle and the right column is the small circle.

### 5.2. The time scale for the porous medium diffusion process

Now we show numerical evidence that the porous medium diffusion process really takes place in the  $O(\varepsilon^{-2})$  time scale, as predicted by (2.10)–(2.12). In the simulation of a two-circle system, once the two circles reach their quasi-equilibrium states, since surface diffusion only changes the shape of each circle and does not provide communication between the two circles, the disappearance of the small circle is essentially determined by the porous medium diffusion process in the background. Hence the time it takes for the small circle to disappear is a good estimate of the time scale in which the porous medium

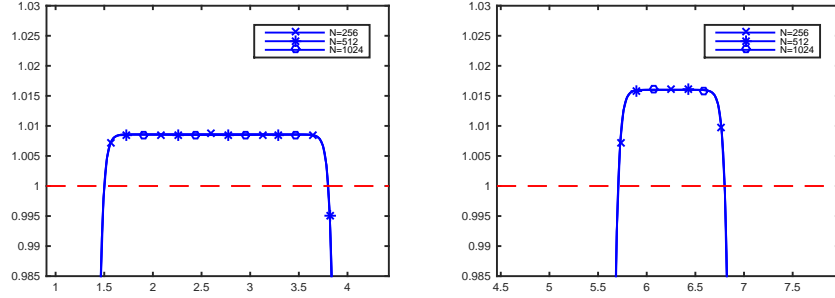


Figure 12:  $M(u) = |1 - u^2|$ , two circles) Comparison of the zooms of the vertical cross sections of  $u$  along the diagonal direction  $y = x$  of the domain  $\Omega$ , at  $t = 100$ , with different space resolution corresponding to  $N = 256, 512$  and  $1024$  with  $\Delta t = 1 \times 10^{-4}$ . There is no visible difference for the three cases.

diffusion process takes place. In Table 1 we list different values of  $\varepsilon$  and the time for the small circle to disappear. We take four values of  $\varepsilon$  which form a geometric series with ratio  $1/\sqrt{2}$ . If the porous medium diffusion process takes place in the  $O(\varepsilon^{-2})$  time scale, then the time that takes for the small circle to disappear should be a geometric series of ratio 2. Considering that for smaller values of  $\varepsilon$ , it takes longer for the system to go through the initial process to reach the quasi-equilibrium state, the data in Table 1 agrees with the theoretical prediction of the time scale for the porous medium diffusion process.

As a by-product, we compare the final equilibrium state, which consists of the surviving big circle, by comparing the maximum and minimum values of  $u$  corresponding to different  $\varepsilon$  values. In our setting in this section, since the positive phase occupies 19% of the system and the domain is  $[0, 2\pi]^2$ , the final radius of the surviving big circle is determined by

$$\pi r^2 = 0.19 \times 4\pi^2, \quad (5.2)$$

or  $r = 1.5452$ . As discussed in Section 2, the two-sided degenerate Cahn-Hilliard equation has the same equilibrium state as the Cahn-Hilliard equation with constant mobility. Theoretically the maximum and minimum of  $u$  are attained inside and outside the big circle, respectively. By (2.7) and (2.9), they satisfy

$$u_{\max} = 1 + \frac{\varepsilon S}{2r} + O(\varepsilon^2) = 1 + 0.1524\varepsilon + O(\varepsilon^2), \quad (5.3)$$

$$u_{\min} = -1 + \frac{\varepsilon S}{2r} + O(\varepsilon^2) = -1 + 0.1524\varepsilon + O(\varepsilon^2). \quad (5.4)$$

Our numerical results are in rows #5 and #6 of Table 1 and they agree with the above theoretical predictions.

### 5.3. Coarsening rates for C-H equation with a two-sided degenerate mobility

There have been many numerical simulations for the two-sided degenerate Cahn-Hilliard equation, but estimates on the coarsening rate have been in the

$\varepsilon$ value	0.0707	0.05	0.0354	0.025
$t$ value when the small circle disappears	410	942	2096	4540
$t$ value when the simulation is terminated	600	1200	2400	4800
$\frac{\varepsilon S}{2r}$	0.0108	0.0076	0.0054	0.0038
$u_{\max}$	1.0107	1.0076	1.0054	1.0039
$u_{\min}$	-0.9889	-0.9922	-0.9945	-0.9961

Table 1: The time needed for the small circle to disappear.

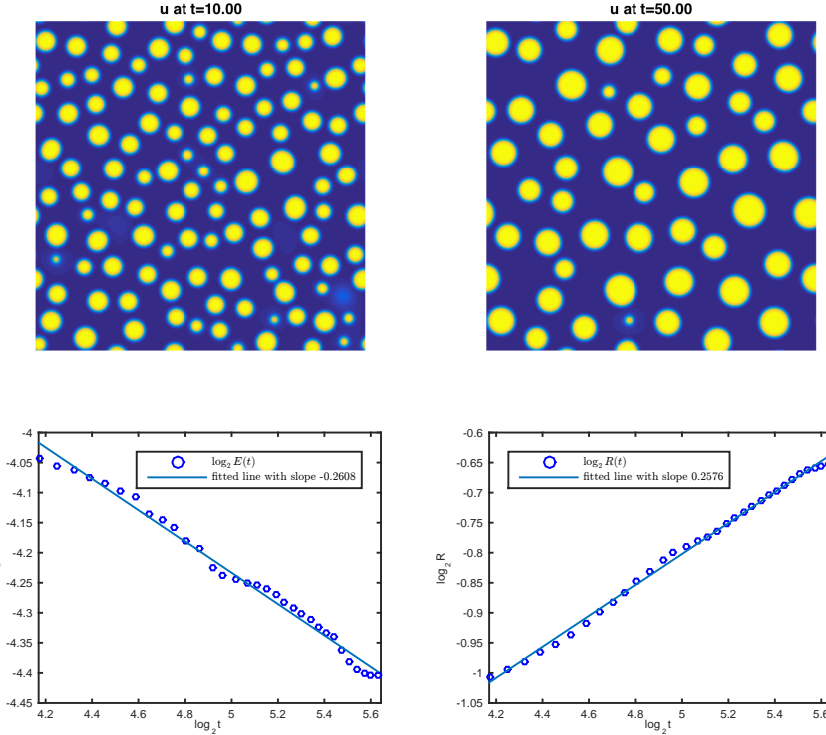


Figure 13: ( $M(u) = |1 - u^2|$ ,  $\varphi = 25\%$ ,  $\Omega = [0, 4\pi]^2$ ,  $\varepsilon = 0.05$ ,  $N = 1024$ ,  $\Delta t = 5 \times 10^{-6}$ .) Morphological patterns at  $t = 10$  (top left) and  $t = 50$  (top right),  $\log_2 \bar{E}(t)$  vs.  $\log_2 t$  (bottom left) and  $\log_2 R(t)$  vs.  $\log_2 t$  (bottom right). Coarsening is mediated through the porous medium diffusion fields in both phases, together with surface diffusion along the interface.

critical case when the positive phase occupies half of the system ( $\varphi = 0.5$ ), see, e.g., [55] (There were simulations in off critical cases for a double-obstacle problem [3]). Since the key feature of our sharp-interface model (2.10)–(2.12) is the existence of a porous medium diffusion process in both phases and that

coarsening occurs even if the interface consists of disjoint pieces, we do a simulation for an off-critical case when the positive phase occupies a small fraction ( $\varphi = 25\%$ ) of the system. The domain is  $\Omega = [0, 4\pi]^2$  with  $N = 1024$ .

The numerical scheme is stable for relatively big time steps but for accuracy considerations, we take  $\Delta t = 5 \times 10^{-6}$ . Indeed we took  $\Delta t = 2.5 \times 10^{-6}$  for  $t$  from 0 to 29 and changed  $\Delta t$  to  $5 \times 10^{-6}$  when realizing that  $2.5 \times 10^{-6}$  was in fact smaller than necessary. In the top of Fig. 13, we show the morphologies of  $u$  at  $t = 10$  and  $t = 50$ , respectively. During the evolution, collisions of droplets are very rare.

The bottom left of Fig. 13 shows the plot of  $\log_2 \bar{E}(t)$  vs.  $\log_2 t$  for  $t \in [18, 50]$ . The linear least square fitting shows that the data can be approximated by a straight line with slope  $-0.2608$ , very close to our theoretical value  $-0.25$ , indicating that the coarsening rate is  $l \sim ct^{1/4}$ . The bottom right of Fig. 13 shows the plot of  $\log_2 R(t)$  vs.  $\log_2 t$ , which is fitted by a straight line of slope  $0.2576$  using least square method, again confirming the coarsening rate  $l \sim ct^{1/4}$ .

## 6. Simulations with a one-sided degenerate mobility $M(u) = |1 + u|$

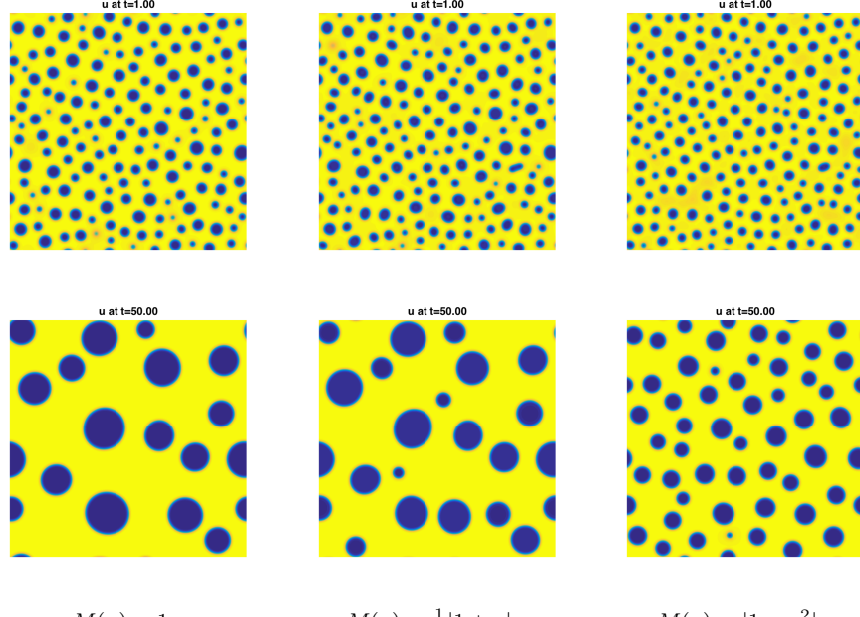
To study the differences in dynamics caused by different diffusion mobilities, we numerically solve the Cahn-Hilliard equation (2.1) with constant mobility  $M(u) = 1$ , one-sided degenerate mobility  $M(u) = \frac{1}{2}|1 + u|$ , and two-sided degenerate mobility  $M(u) = |1 - u^2|$  on the same mesh grid and the same initial value. Since volume fraction of the positive phase is a critical factor for the separation of time scales for the case of one-sided degenerate mobility  $M(u) = \frac{1}{2}|1 + u|$ , we consider three scenarios.

When studying coarsening of a system analytically, one essential assumption is that the system approaches a self-similar morphology. Without such an assumption, one can only consider upper bounds on coarsening rates [26, 35, 36]. Although self-similarity may not be universally true, it is expected to be true generically [34]. Before approaching the self-similar stage, there may be transient behaviors in the early stage of coarsening [20], with a coarsening rate slower than predicted by scaling argument based on the geometric interface motion laws.

So for systems that are large enough, the self-similar morphology generically should be expected in an intermediate regime, after the initial transient regime, and before the later regime where the dynamics settles down to the equilibrium state. Following this guideline, in the following we show numerical evidences for the coarsening rates for the Cahn-Hilliard equation (2.1) with a one-sided degenerate mobility  $M(u) = \frac{1}{2}|1 + u|$ .

### 6.1. Scenario 1: Positive phase occupying $\varphi = 75\%$ of the system

The first scenario is when the positive phase occupies  $\varphi = 75\%$  of the system. We take  $\Omega = [0, 4\pi]^2$  and  $N = 1024$ ,  $\varepsilon = 0.05$ . The initial value  $u_{10}$  is taken as a constant  $\bar{u}_{10} = 2\varphi - 1 = 0.5$ , with a perturbation that is uniformly distributed in  $[-0.2, 0.2]$ . Due to stability and accuracy considerations, we have to take different time steps for different diffusion mobilities.



$$M(u) = 1$$

$$M(u) = \frac{1}{2}|1+u|$$

$$M(u) = |1-u^2|$$

Figure 14: ( $\varphi = 75\%$ ,  $\Omega = [0, 4\pi]^2$ ,  $N = 1024$ ) Comparison of morphological differences caused by different diffusion mobilities. The initial values are the same. Top row:  $t = 1$ ; Bottom row:  $t = 50$ . (left column)  $M(u) = 1$ ; (middle column)  $M(u) = \frac{1}{2}|1+u|$ ; (right column)  $M(u) = |1-u^2|$ .

- For  $M(u) = 1$ , we take  $\Delta t = 1 \times 10^{-5}$ . In fact this is unnecessarily small. We can take  $\Delta t = 1 \times 10^{-4}$  with enough accuracy and without losing stability.
- For  $M(u) = \frac{1}{2}|1+u|$ , we take  $\Delta t = 5 \times 10^{-6}$ . Numerical stability prevents us from using bigger time steps.
- For  $M(u) = |1-u^2|$ , we take  $\Delta t = 5 \times 10^{-6}$ . The numerical scheme remains stable for much bigger time steps but it appears that accuracy can be an issue.

We denote the solutions for the three cases by  $u_1^{\text{const}}$ ,  $u_1^{\text{onesided}}$ ,  $u_1^{\text{twosided}}$ , respectively.

#### 6.1.1. Morphological evolution ( $\varphi = 75\%$ )

Fig. 14 shows the morphologies of the system at  $t = 1$  and  $t = 50$ , for the three different diffusion mobilities. We can see that at  $t = 1$ , the morphologies appear to be very similar for the three mobilities. At  $t = 50$ , it is obvious that the characteristic length scale, which can be defined as the average size of droplets, is very small for  $M(u) = |1-u^2|$ . The average size of droplets is biggest for  $M(u) = 1$  and slightly smaller for  $M(u) = \frac{1}{2}|1+u|$ . This is

consistent with our discussion of coarsening dynamics in Section 2. For the two-sided degenerate mobility  $M(u) = |1 - u^2|$ , coarsening always occurs in a much slower time scale  $t_2 = O(\varepsilon^{-2})$ , with a slower coarsening rate  $l(t_2) \sim c_3 t_2^{1/4}$ . On the contrary, for the constant mobility Cahn-Hilliard equation, the coarsening dynamics occurs always in the  $t_1 = O(\varepsilon^{-1})$  time scale with a coarsening rate  $l(t_1) \sim c_1 t_1^{1/3}$ . The coarsening is mediated through a diffusion field in both bulk phases (2.4)–(2.6). For the case  $M(u) = \frac{1}{2}|1 + u|$ , since the positive phase is connected, the coarsening dynamics also occurs in the  $t_1$  time scale with a coarsening rate  $l(t_1) \sim c_2 t_1^{1/3}$ . But it is mediated by the diffusion field in the positive phase (2.14)–(2.16). Compared with the constant mobility case, the lack of contribution from the negative phase gives a slightly slower dissipation rate of interfacial area.

#### 6.1.2. Coarsening rate ( $\varphi = 75\%$ )

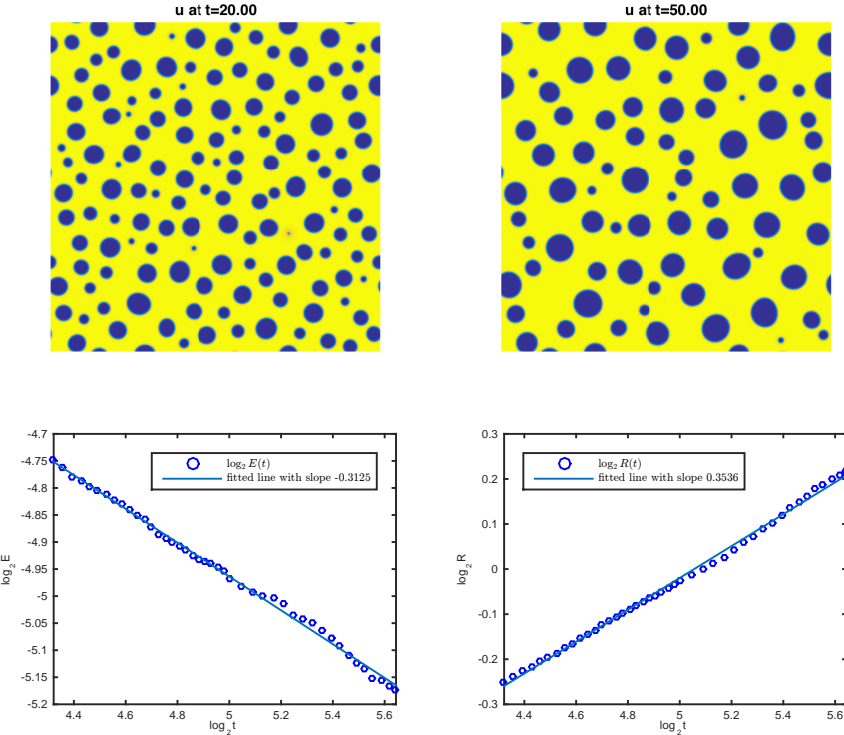


Figure 15: ( $M(u) = \frac{1}{2}|1 + u|$ ,  $\varphi = 75\%$ ,  $\Omega = [0, 8\pi]^2$ ,  $\varepsilon = 0.05$ ,  $N = 2048$ ,  $\Delta t = 5 \times 10^{-6}$ .) Morphological patterns at  $t = 20$  (top left) and  $t = 50$  (top right),  $\log_2 \bar{E}(t)$  vs.  $\log_2 t$  (bottom left) and  $\log_2 R(t)$  vs.  $\log_2 t$  (bottom right). Coarsening is mediated through the Hele-Shaw diffusion field in the positive phase.

In this case, the negative phase consists of near spherical pieces. Collision is rare. To further reduce the finite size effect, in Fig. 15 we show the simulation

results for a bigger domain  $\Omega = [0, 8\pi]^2$  with  $N = 2048$ . In the top of Fig. 15 we show the evolution of the morphological patterns at  $t = 20$  and  $t = 50$ . Since the positive phase is connected, the  $t_1 = O(\varepsilon^{-1})$  dynamics dominates and the coarsening process is mediated through the one-sided Hele-Shaw model (2.14)–(2.16), with a predicted coarsening rate  $l \sim t^{1/3}$ . The bottom left and bottom right of Fig. 15 show the plots of  $\log_2 \bar{E}(t)$  and  $\log_2 R(t)$  vs.  $\log_2 t$ , respectively, for  $t \in [20, 50]$ . It is clear that they can be fitted by straight lines, with slopes  $-0.3125$  and  $0.3536$ , respectively, confirming the predicted coarsening rate with a power  $\alpha = 3$ . Since the coarsening of CH equation with constant mobility is well known, it is not necessary to show our simulations for it with the same initial data. Together with the results in Section 5, we summarize the comparison of the degenerate diffusional mobilities as follows.

**Result 2.** *If the positive phase occupies a big fraction of the system ( $\varphi = 75\%$ ),*

- (i) . for  $M(u) = 1$ , the coarsening rate is  $l(t) \sim c_{11}t^{1/3}$ ;
- (ii) . for  $M(u) = \frac{1}{2}|1+u|$ , the coarsening rate is  $l(t) \sim c_{21}t^{1/3}$ , with  $c_{21} < c_{11}$ ;
- (iii) . for  $M(u) = |1-u^2|$ , the coarsening rate is  $l(t) \sim c_{31}t^{1/4}$ .

### 6.2. Scenario 2: Positive phase occupying $\varphi = 50\%$ of the system

The second scenario is when the positive phase occupies  $\varphi = 50\%$  of the system. We take  $\Omega = [0, 8\pi]^2$  and  $N = 2048$ ,  $\varepsilon = 0.05$ . The initial value  $u_{20}$  is a constant  $\bar{u}_{20} = 2\varphi - 1 = 0$ , with a perturbation uniformly distributed in  $[-0.2, 0.2]$ .

- For  $M(u) = 1$ , we take  $\Delta t = 1 \times 10^{-5}$ . Again this is unnecessarily small. We can take  $\Delta t = 1 \times 10^{-4}$ .
- For  $M(u) = \frac{1}{2}|1+u|$ , we take  $\Delta t = 2.5 \times 10^{-6}$ . We have to take a smaller time step than in scenario one due to numerical stability restraints.
- For  $M(u) = |1-u^2|$ , we take  $\Delta t = 5 \times 10^{-6}$ .

#### 6.2.1. Morphological evolution ( $\varphi = 50\%$ )

Fig. 16 shows the morphologies at  $t = 1$  and  $t = 20$  for the three diffusion mobilities. This time even at  $t = 1$  we already see some minor differences in morphologies. The differences are much more apparent at  $t = 20$ . In this scenario it seems visually easier to estimate the coarsening rate by considering the dissipation rate of the Cahn-Hilliard energy, which is proportional to the interfacial area. Apparently the interfacial area is biggest for  $M(u) = |1-u^2|$ , as a consequence of a slower coarsening rate in a slower time scale. As for the interfacial areas for  $M(u) = 1$  and  $M(u) = \frac{1}{2}|1+u|$ , the difference between these two is pretty small, even though the former is slightly smaller. This can again be explained by the same argument for the first scenario.

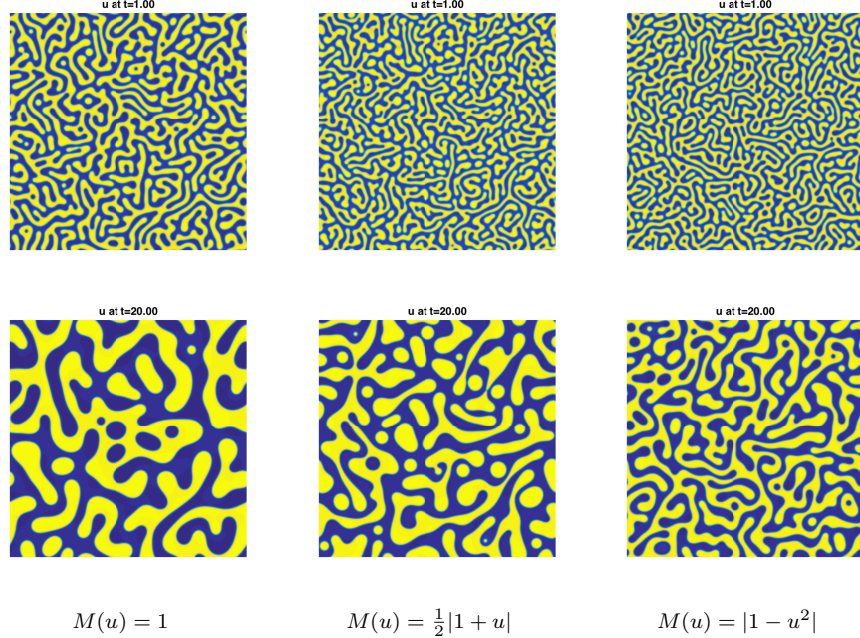


Figure 16: ( $\varphi = 50\%$ ,  $\Omega = [0, 8\pi]^2$ ,  $N = 2048$ ) Comparison of morphological differences caused by different diffusion mobilities. The initial values are the same. Top row:  $t = 1$ ; Bottom row:  $t = 20$ . (left column)  $M(u) = 1$ ; (middle column)  $M(u) = \frac{1}{2}|1+u|$ ; (right column)  $M(u) = |1-u^2|$ .

### 6.2.2. Coarsening rate ( $\varphi = 50\%$ )

In this case, both positive and negative phases are largely connected. There are some isolated pieces of positive phases but they are just a minor part of the system. In addition, during evolution these isolated pieces collide with neighboring structures. Consequently, without considering the fast collision processes, the  $t_1$  dynamics in the positive phase dominates and coarsening is essentially mediated through the one-sided Hele-Shaw problem (2.14)–(2.16) in the positive phase. The top of Fig. 17 shows the morphology at  $t = 1$  and  $t = 10$ . The coarsening rate is again the predicted  $l \sim t^{1/3}$ , and is evidenced by the slope  $-0.3232$  of the fitted line for  $\log_2 \bar{E}(t)$  vs.  $\log t$  in the bottom left of Fig. 17, and the slope of  $0.3382$  of the fitted line for  $\log_2 R(t)$  vs.  $\log_2 t$  in the bottom right of Fig. 17.

Compared with the Cahn-Hilliard equation with constant mobility  $M(u) = 1$ , and in combination with the well-known results for the Cahn-Hilliard equation with two-sided degenerate mobility (e.g., [55]), we numerically confirm the following coarsening rates in the case when the positive phase occupies half of the system.

**Result 3.** *If the positive phase occupies half of the system ( $\varphi = 50\%$ ),*

- (i) . for  $M(u) = 1$ , the coarsening rate is  $l(t) \sim c_{12}t^{1/3}$ ;

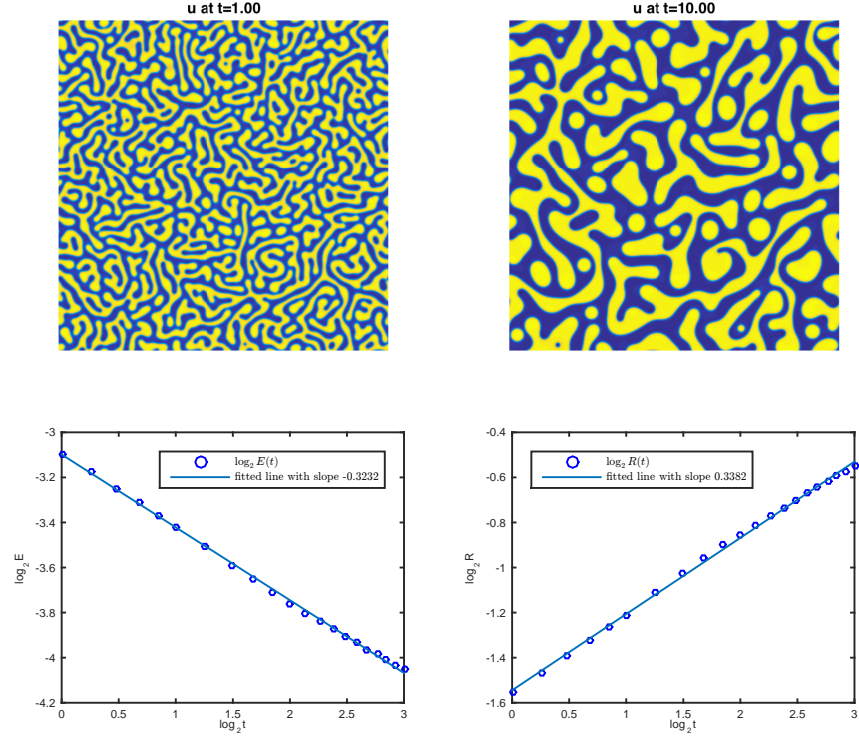


Figure 17: ( $M(u) = \frac{1}{2}|1+u|$ ,  $\varphi = 50\%$ ,  $\Omega = [0, 8\pi]^2$ ,  $\varepsilon = 0.05$ ,  $N = 2048$ ,  $\Delta t = 2.5 \times 10^{-6}$ .) Morphological patterns at  $t = 1$  (top left) and  $t = 10$  (top right),  $\log_2 \bar{E}(t)$  vs.  $\log_2 t$  (bottom left) and  $\log_2 R(t)$  vs.  $\log_2 t$  (bottom right). Coarsening is essentially mediated through the Hele-Shaw diffusion field in each branch of the positive phase.

- (ii) . for  $M(u) = \frac{1}{2}|1+u|$ , the coarsening rate is  $l(t) \sim c_{22}t^{1/3}$ , with  $c_{22} < c_{12}$ .
- (iii) . for  $M(u) = |1-u^2|$ , the coarsening rate is  $l(t) \sim c_{32}t^{1/4}$ .

### 6.3. Scenario 3: Positive phase occupying $\varphi = 25\%$ of the system

The third scenario is when the positive phase occupies  $\varphi = 25\%$  of the system. We again take  $\Omega = [0, 4\pi]^2$  and  $N = 1024$ ,  $\varepsilon = 0.05$ . Since this is a counterpart of scenario one, due to symmetry we take the initial value  $u_{30}$  to be the negative of that of scenario one, that is

$$u_{30} = -u_{10}.$$

In this setting, since the double-well potential is an even function, the solution  $u_3^{\text{const}}$  for the constant diffusion mobility  $M(u) = 1$  and  $u_3^{\text{twosided}}$  for the two-sided degenerate mobility  $M(u) = |1-u^2|$  are, respectively, the negative of the solutions in scenario one, that is

$$u_3^{\text{const}} = -u_1^{\text{const}}, \quad u_3^{\text{twosided}} = -u_1^{\text{twosided}}.$$

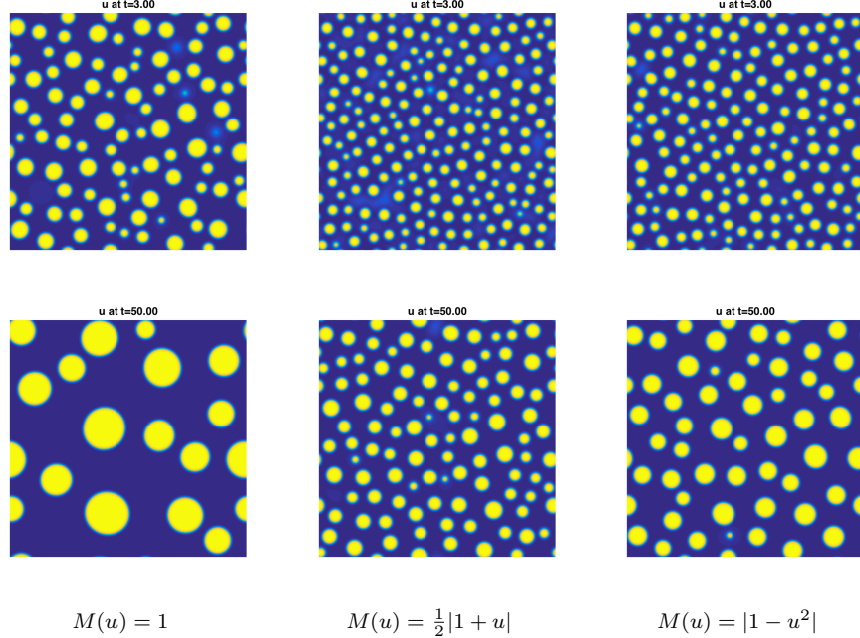


Figure 18: ( $\varphi = 25\%$ ,  $\Omega = [0, 4\pi]^2$ ,  $N = 1024$ ) Comparison of morphological differences caused by different diffusion mobilities. The initial values are the same. Top row:  $t = 3$ ; Bottom row:  $t = 50$ . (left column)  $M(u) = 1$ ; (middle column)  $M(u) = \frac{1}{2}|1+u|$ ; (right column)  $M(u) = |1-u^2|$ .

Consequently in this scenario, the only additional simulation we need to carry out is for the asymmetric one-sided degenerate mobility  $M(u) = \frac{1}{2}|1+u|$ .

- For  $M(u) = \frac{1}{2}|1+u|$ , we take  $\Delta u = 1 \times 10^{-6}$ . This time step is much smaller than that in scenarios one and two, due to numerical stability restraints.

#### 6.3.1. Morphological evolution ( $\varphi = 25\%$ )

Fig. 18 shows the morphologies at  $t = 3$  and  $t = 50$  for the three mobilities. It can be seen that the one-sided degenerate case exhibits the slowest coarsening rate, measured in terms of the average size of droplets. The constant mobility case exhibits the fastest coarsening rate since it follows a  $1/3$  power law in a faster time scale  $t_1 = O(\varepsilon^{-1})$ , while the one-sided and two-sided degenerate mobility cases both follow a  $1/4$  power law in a slower time scale  $t_2 = O(\varepsilon^{-2})$ . The reason for the one-sided degenerate case to be the slowest is that, according to (2.18)–(2.20), the one-sided degenerate case is solely mediated through the porous medium diffusion process in the negative phase, while the two-sided degenerate case is mediated through surface diffusion, combined with porous medium diffusion processes in both phases.

### 6.3.2. Coarsening rate ( $\varphi = 25\%$ )

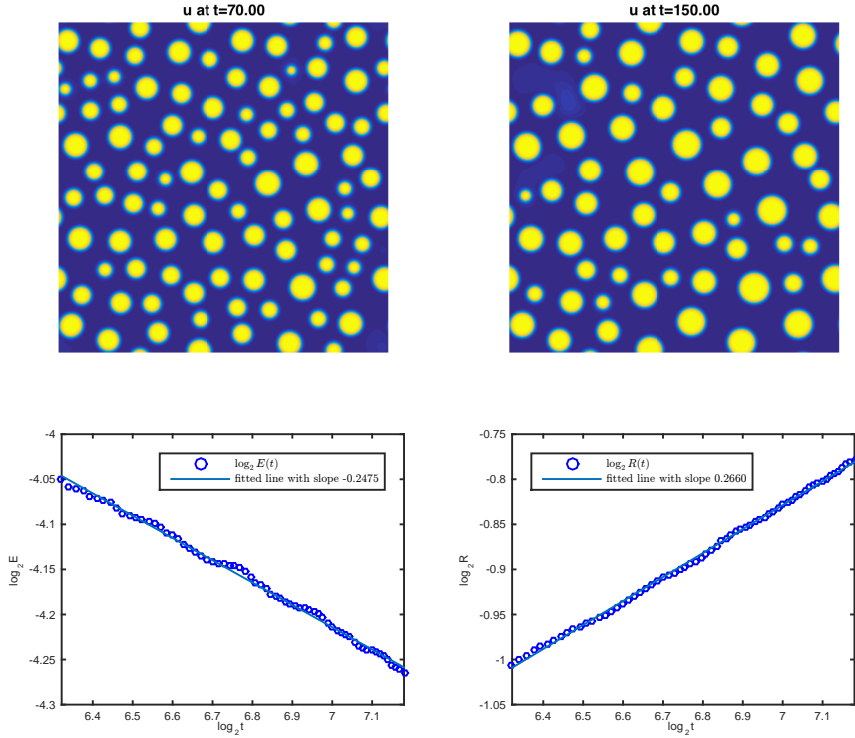


Figure 19: ( $M(u) = \frac{1}{2}|1+u|$ ,  $\varphi = 25\%$ ,  $\Omega = [0, 4\pi]^2$ ,  $\varepsilon = 0.05$ ,  $N = 1024$ ,  $\Delta t = 1 \times 10^{-6}$ .) Morphological patterns at  $t = 70$  (top left) and  $t = 150$  (top right),  $\log_2 E(t)$  vs.  $\log_2 t$  (bottom left) and  $\log_2 R(t)$  vs.  $\log_2 t$  (bottom right). Coarsening is mediated through the porous medium diffusion field in the negative phase.

In this case, the positive phase breaks into disjoint nearly spherical pieces and the coarsening is mediated through the one-sided quasi-stationary porous medium diffusion process (2.18) – (2.20) in the negative phase, in the slower  $t_2 = O(\varepsilon^{-2})$  time scale. The coarsening rate is  $l \sim t_2^{1/4}$  and it is a much slower process.

Numerical experiments show that we need a smaller time step  $\Delta t = 1 \times 10^{-6}$  for this case to retain the stability of the numerical scheme. As a consequence, the computation becomes very time consuming. The top of Fig. 19 shows the morphologies at  $t = 70$  and  $t = 150$ . The graphs of  $\log_2 E(t)$  vs.  $\log_2 t$  in the bottom left of Fig. 19 and  $\log_2 R(t)$  vs.  $\log_2 t$  in the bottom right of Fig. 19 can be approximated using least square method by straight lines with slopes  $-0.2475$  and  $0.2660$ , respectively, confirming the predicted coarsening rate  $l \sim t_2^{1/4}$ . Again in the plots we see meandering along the reference straight lines, but in average the reference lines remain good approximations of the plots. Such meandering and staircasing behaviors are also observed in the coarsening

of thin liquid films [22].

Compared with the solution to the Cahn-Hilliard equation with two-sided degenerate mobility  $M(u) = |1 - u^2|$  with the same initial data (Fig. 13), we obtain the following result about coarsening rates in the case when the positive phase occupies a minor part of the system.

**Result 4.** *If the positive phase occupies a small fraction of the system ( $\varphi = 25\%$ ),*

- (i) . for  $M(u) = 1$ , the coarsening rate is  $l(t) \sim c_{13}t^{1/3}$ ;
- (ii) . for  $M(u) = \frac{1}{2}|1 + u|$ , the coarsening rate is  $l(t) \sim c_{23}t^{1/4}$ , with  $c_{23} < c_{33}$ ;
- (iii) . for  $M(u) = |1 - u^2|$ , the coarsening rate is  $l(t) \sim c_{33}t^{1/4}$ .

#### 6.4. About the accuracy of time discretization

Since the main goal of this work is to accurately simulate the coarsening dynamics, in this subsection we show evidence that the time steps we use are small enough to guarantee the accuracy. Since the most time consuming simulation is Scenario 3 in Section 6.3 of the one-sided degenerate case, to show that  $\Delta t = 1 \times 10^{-6}$  provides sufficient accuracy, we compare the results with a simulation using  $\Delta t = 5 \times 10^{-7}$ . More precisely, let

$u$  be the numerical solution using  $\Delta t = 1 \times 10^{-6}$ ; and

$\tilde{u}$  be the numerical solution using  $\Delta t = 5 \times 10^{-7}$ , for  $t \in [10, 30]$ , with initial value  $\tilde{u}(10) = u(10)$ .

To measure the difference between  $u$  and  $\tilde{u}$ , we calculate the  $L^\infty$  and  $L^2$  norms of  $u - \tilde{u}$  by

$$err_\infty(t) := \max_{x \in \Omega} |u(x, t) - \tilde{u}(x, t)|, \quad (6.1)$$

$$err_2(t) := \left( \frac{1}{|\Omega|} \int_{\Omega} |u(x, t) - \tilde{u}(x, t)|^2 dx \right)^{1/2} \quad (6.2)$$

and plot them in Figure 20. It can be seen that  $err_\infty(t) = O(10^{-5})$  and  $err_2(t) = O(10^{-7})$  for  $t \in [10, 30]$ .

In addition, we measure the difference between  $u$  and  $\tilde{u}$  by their energy. Let  $\bar{E}(u)$  and  $\bar{E}(\tilde{u})$  be the energy corresponding to solutions  $u(t)$  and  $\tilde{u}(t)$  for  $t \in [10, 30]$ , respectively. Figure 21 shows the plots of  $\bar{E}(u)$  vs.  $t$ ,  $\bar{E}(\tilde{u})$  vs.  $t$ , and their difference  $|\bar{E}(u) - \bar{E}(\tilde{u})|$  vs.  $t$ . The energy difference caused by the two choices of time steps is of the order  $O(10^{-9})$ . By these comparisons, we see that the difference between choosing  $\Delta t = 1^{-6}$  and choosing  $\Delta t = 5 \times 10^{-7}$  is very small. Hence our simulation in Section 6.3 is sufficiently accurate.

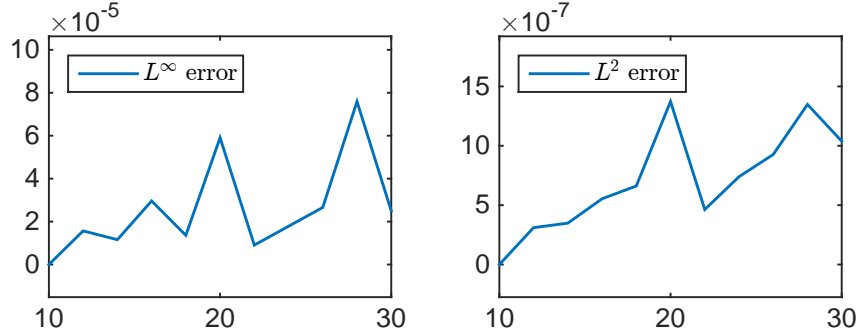


Figure 20: The difference between  $u(x, t)$  and  $\tilde{u}(x, t)$ , measured by the  $L^\infty$  norm (left), and the averaged  $L^2$  norm (right).

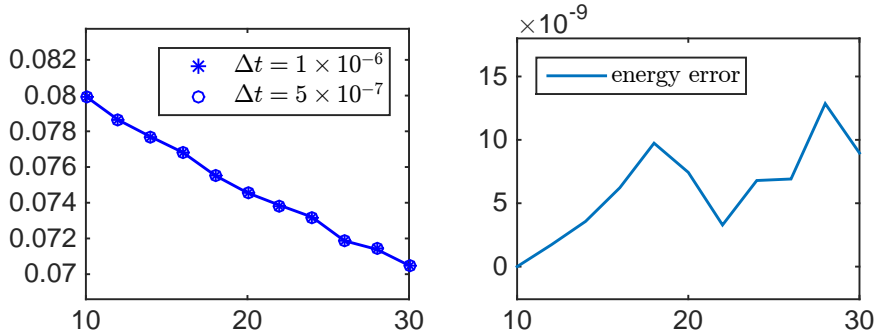


Figure 21:  $\bar{E}(u)$  and  $\bar{E}(\tilde{u})$  vs. time (left) and  $|\bar{E}(u) - \bar{E}(\tilde{u})|$  vs. time (right).

## 7. Discussion

Numerical experiments reported in the above further substantiate earlier predictions given in [11, 12] on the coarsening mechanism and coarsening rates governed by the Cahn-Hilliard models. We take note, in particular, of the consistency between numerical observations and theoretical predictions when the underlying microstructure evolution enters the appropriate asymptotic regime. The latter regime corresponds to an essential assumption that the system approaches a self-similar morphology [34]. Meanwhile, it is also interesting to make some observations on the transient solution behavior [20] in the pre-asymptotic regime.

We focus on the one-sided degenerate case here. In Fig. 22, we plot  $\log_2 \bar{E}(t)$  and  $\log_2 R(t)$  against  $\log_2 t$  for the two cases of one-sided mobilities  $M(u) = \frac{1}{2}|1+u|$  with positive volume fractions at 25% and 75% respectively.

The plots in Fig. 22 clearly show the appearance of persistent initial transition periods, a pattern that does not show in the case corresponding to the 50% volume fraction case given in Fig. 17. For the latter case, there is literally no transition regime. We can interpret this observation based on the understanding

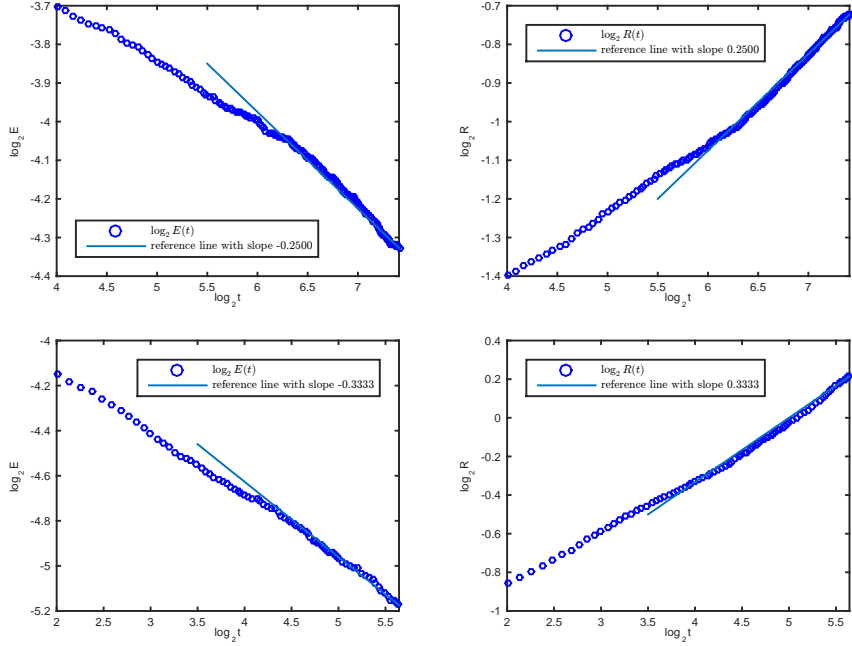


Figure 22: ( $M(u) = \frac{1}{2}|1+u|$ ) Pre-asymptotic regime: Top row:  $\varphi = 25\%$ ,  $\Omega = [0, 4\pi]^2$ ,  $N = 1024$ ; bottom row:  $\varphi = 75\%$ ,  $\Omega = [0, 8\pi]^2$ ,  $N = 2048$ . Left column:  $\log_2 \bar{E}(t)$  vs.  $\log_2 t$  and Right column:  $\log_2 R(t)$  vs.  $\log_2 t$ .

that the 50% volume fraction case describes an almost instantaneous spinodal decomposition. For small volume fraction cases, the initial phase separation is due to nucleation which makes a difference. As documented in earlier sections, for positive volume fractions that are larger than 50%, the coarsening rates are expected to take value 1/3, once they are in the self-similar regime, while for small positive volume fraction cases including the 25% example, the coarsening rates are 1/4.

For cases with a 30-35% positive phase, different transition dynamics may result. Rather than having only spherical domains as in the 25% case, the positive phase in a 35% case typically consists of many disjoint pieces but with more complicated morphology. There is no clear separation of time scale in the dynamics, since the diffusion in the positive phase does not really equilibrate. Still, the disjoint positive domains communicate only through the slower porous medium diffusion in the negative phase, until they coalesce, after which diffusion in the positive phase starts to take control. This leads to the possibility of a cross-over of coarsening rates, say between 1/4 and 1/3. Given that the exiting theoretical analysis does not cover such a scenario, a careful study of such cross-over is then left as a question for more future research.

Through the illustrative simulations shown here, the present work serves to inform the community the delicate nature of choosing the proper mobilities and

free energy potentials in large scale phase field simulations in order to capture the fine details of the material microstructure evolution and to make correct predictions on the statistics. In practice, microstructure evolutions also involve other important aspects that have not been fully incorporated in our study. For example, more complex systems may involve multiple phases and order parameters. The effect of long range elastic interactions also plays important roles in coarsening dynamics. More future works are needed to advance both theoretical analysis and computational modeling of microstructure morphology in real materials systems.

### Acknowledgments

S. D. was supported in part by US NSF grant DMS-1411438, and Q. D. was supported in part by US NSF grant DMS-1318586.

- [1] N. Alikakos, P. Bates, and X. Chen. Convergence of the Cahn-Hilliard equation to the Hele-Shaw model. *Arch. Rat. Mech. Anal.*, 128:165–205, 1994.
- [2] A. J. Arnett and V. Ozolins. Trans-interface diffusion-controlled coarsening. *Nat. Mater.*, 4:309–316, April 2005.
- [3] L. Bañas, A. Novick-Cohen, and R. Nürnberg. The degenerate and non-degenerate deep quench obstacle problem: A numerical comparison. *Networks and Heterogeneous Media*, 8(1):37–64, 2013.
- [4] J. W. Barrett, J. F. Blowey, and H. Garcke. Finite element approximation of the Cahn–Hilliard equation with degenerate mobility. *SIAM Journal on Numerical Analysis*, 37(1):286–318, 1999.
- [5] A. J. Bray and C. L. Emmott. Lifshitz-Slyozov scaling for late-stage coarsening with an order-parameter-dependent mobility. *Phys. Rev. B*, 52:R685–R688, 1995.
- [6] J. W. Cahn and J. E. Taylor. Surface motion by surface diffusion. *Acta. Metall. Mater.*, 42:1045–1063, 1994.
- [7] H. Ceniceros and C. García-Cervera. A new approach for the numerical solution of diffusion equations with variable and degenerate mobility. *J. Comput. Phys.*, 246:1–10, 2013.
- [8] L.-Q. Chen and J. Shen. Applications of semi-implicit fourier-spectral method to phase field equations. *Computer Physics Communications*, 108(2):147–158, 1998.
- [9] X. Chen. The Hele-Shaw problem and area-preserving curve-shortening motions. *Arch. Rational Mech. Anal.*, 123:117–151, 1993.

- [10] J. G. Conley, M. E. Fine, and J. R. Weertman. Effect of lattice disregistry variation on the late stage phase transformation behavior of precipitates in Ni-Al-Mo alloys. *Acta Metallurgica*, 37(4):1251 – 1263, 1989.
- [11] S. Dai and Q. Du. Motion of interfaces governed by the Cahn-Hilliard equation with highly disparate diffusion mobility. *SIAM J. Appl. Math.*, 72(6):1818–1841, 2012.
- [12] S. Dai and Q. Du. Coarsening mechanism for systems governed by the Cahn-Hilliard equation with degenerate diffusion mobility. *Multiscale Modeling and Simulation*, 12(4):1870–1889, 2014.
- [13] S. Dai and Q. Du. Weak solutions for the Cahn-Hilliard equation with phase-dependent diffusion mobility. *Archive for Rational Mechanics and Analysis*, to appear.
- [14] Q. Du and R. Nicolaides. Numerical analysis of a continuum model of phase transition. *SIAM Journal on Numerical Analysis*, 28(5):1310–1322, 1991.
- [15] C. Elliott and H. Garcke. On the Cahn-Hilliard equation with degenerate mobility. *SIAM J. Math. Anal.*, 27(2):404–423, 1996.
- [16] D. J. Eyre. An unconditionally stable one-step scheme for gradient systems. <http://www.math.utah.edu/~eyre/research/methods/stable.ps>, 1998.
- [17] D. Fan, S. Chen, L.-Q. Chen, and P. Voorhees. Phase-field simulation of 2-D Ostwald ripening in the high volume fraction regime. *Acta Materialia*, 50:1895 – 1907, 2002.
- [18] W. Feng, P. Yu, S. Hu, Z. Liu, Q. Du, and L. Chen. A Fourier spectral moving mesh method for the Cahn–Hilliard equation with elasticity. *Commun. Comput. Phys.*, 5:582–599, 2009.
- [19] X. Feng and A. Prohl. Numerical analysis of the Cahn-Hilliard equation and approximation for the Hele-Shaw problem. *Interfaces and Free Boundaries*, 7(1):1–28, 2005.
- [20] H. Garcke, B. Niethammer, M. Rumpf, and U. Weikard. Transient coarsening behaviour in the Cahn-Hilliard model. *Acta Materialia*, 51:2823–2830, 2003.
- [21] H. Gómez, V. Calo, Y. Bazilevs, and T. Hughes. Isogeometric analysis of the Cahn–Hilliard phase-field model. *Computer Methods in Applied Mechanics and Engineering*, 197(49):4333–4352, 2008.
- [22] M. B. Gratton and T. P. Witelski. Transient and self-similar dynamics in thin film coarsening. *Physica D: Nonlinear Phenomena*, 238(23-24):2380 – 2394, 2009.

- [23] Z. Guan, J. S. Lowengrub, C. Wang, and S. M. Wise. Second order convex splitting schemes for periodic nonlocal Cahn-Hilliard and Allen-Cahn equations. *Journal of Computational Physics*, 277:48–71, 2014.
- [24] F. Guillén-González and G. Tierra. On linear schemes for a Cahn-Hilliard diffuse interface model. *Journal of Computational Physics*, 234:140–171, 2013.
- [25] L. Ju, J. Zhang, and Q. Du. Fast and accurate algorithms for simulating coarsening dynamics of Cahn–Hilliard equations. *Computational Materials Science*, 2015.
- [26] R. V. Kohn and F. Otto. Upper bounds on coarsening rates. *Comm. Math. Phys.*, 229:375–395, 2002.
- [27] T. Kupper and N. Masbaum. Simulation of particle growth and Ostwald ripening via the Cahn-Hilliard equation. *Acta Metallurgica et Materialia*, 42:1847 – 1858, 1994.
- [28] A. M. Lacasta, A. Hernández-Machado, J. M. Sancho, and R. Toral. Domain growth in binary mixtures at low temperature. *Phys Rev. B.*, 45(10):5276–5281, 1992.
- [29] J. S. Langer. Models of pattern formation in first-order phase transitions. *Directions in Condensed Matter Physics*, pages 1549–1564, 1986.
- [30] J. S. Langer, M. Bar-on, and H. D. Miller. New computational method in the theory of spinodal decomposition. *Phys Rev. A*, 11(4):1417–1429, 1975.
- [31] I. M. Lifshitz and V. V. Slyozov. The kinetics of precipitation from supersaturated solid solutions. *J. Phys. Chem. Solids*, 19:35–50, 1961.
- [32] A. Nepomnyashchy. Coarsening versus pattern formation. *Comptes Rendus Physique*, 2015.
- [33] B. Niethammer. Derivation of the LSW theory for Ostwald ripening by homogenization methods. *Arch. Ration. Mech. Anal.*, 147:119–178, 1999.
- [34] B. Niethammer and R. L. Pego. Non-self-similar behavior in the LSW theory of Ostwald ripening. *J. Stat. Phys.*, 95:867–902, 1999.
- [35] A. Novick-Cohen. Upper bounds for coarsening for the deep quench obstacle problem. *Journal of Statistical Physics*, 141(1):142–157, 2010.
- [36] A. Novick-Cohen and A. Shishkov. Upper bounds for coarsening for the degenerate Cahn-Hilliard equation. *Discrete and Continuous Dynamical Systems – Series A*, 25(1):251–272, 2009.
- [37] R. L. Pego. Front migration in the nonlinear Cahn-Hilliard equation. *Proc. Royal Soc. London A*, 442:261–278, 1989.

- [38] R. L. Pego. Lectures on dynamics in models of coarsening and coagulation. In *Dynamics in models of coarsening, coagulation, condensation and quantization*, volume 9 of *Lecture Notes Series, Institute for Mathematical Sciences, National University of Singapore*, 2007.
- [39] S. Puri, A. J. Bray, and J. L. Lebowitz. Phase-separation kinetics in a model with order-parameter-dependent mobility. *Physical Review E*, 56(1):758, 1997.
- [40] T. Rogers and R. Desai. Numerical study of late-stage coarsening for off-critical quenches in the Cahn–Hilliard equation of phase separation. *Phys. Rev. B*, 39:11956–11964, 1989.
- [41] D. N. Seidman, C. K. Sudbrack, and K. E. Yoon. The use of 3-D atom-probe tomography to study nickel-based superalloys. *JOM*, 58(12):34–39, 2006.
- [42] J. Shen and X. Yang. Numerical approximations of Allen–Cahn and Cahn–Hilliard equations. *Discrete Continuous Dynamical Syst. A*, 28:1669–1691, 2010.
- [43] G. Sheng, T. Wang, Q. Du, K.G. Wang, Z.-K. Liu, and L.-Q. Chen. Coarsening kinetics of a two phase mixture with highly disparate diffusion mobility. *Commun. Comput. Phys.*, 8(2):249–264, 2010.
- [44] J. Shin, D. Jeong, and J. Kim. A conservative numerical method for the Cahn–Hilliard equation in complex domains. *Journal of Computational Physics*, 230(19):7441–7455, 2011.
- [45] J. E. Taylor and J. W. Cahn. Linking anisotropic sharp and diffuse surface motion laws via gradient flows. *J. Stat. Phys.*, 77(1/2):183–197, 1994.
- [46] K. Thornton, J. Ågren, and P. Voorhees. Modelling the evolution of phase boundaries in solids at the meso-and nano-scales. *Acta Materialia*, 51(19):5675–5710, 2003.
- [47] P. W. Voorhees. The theory of Ostwald ripening. *J. Stat. Phys.*, 38(1/2):231–252, 1985.
- [48] C. Wagner. Theorie der Alterung von Niederschlägen durch Umlösen. *Z. Elektrochem.*, 65:581–594, 1961.
- [49] T. Wang, G. Sheng, Z.-K. Liu, and L.-Q. Chen. Coarsening kinetics of  $\gamma'$  precipitates in the Ni-Al-Mo system. *Acta Materialia*, 56(19):5544 – 5551, 2008.
- [50] S. Wise, J. Kim, and J. Lowengrub. Solving the regularized, strongly anisotropic Cahn–Hilliard equation by an adaptive nonlinear multigrid method. *Journal of Computational Physics*, 226(1):414–446, 2007.

- [51] Y. Xia, Y. Xu, and C.-W. Shu. Local discontinuous Galerkin methods for the Cahn–Hilliard type equations. *Journal of Computational Physics*, 227(1):472–491, 2007.
- [52] J. Yin. On the existence of nonnegative continuous solutions of the Cahn–Hilliard equation. *Journal of Differential Equations*, 97:310–327, 1992.
- [53] J. Zhang and Q. Du. Numerical studies of discrete approximations to the Allen-Cahn equation in the sharp interface limit. *SIAM Journal on Scientific Computing*, 31(4):3042–3063, 2009.
- [54] L. Zhang, M. R. Tonks, D. Gaston, J. W. Peterson, D. Andrs, P. C. Millett, and B. S. Biner. A quantitative comparison between  $C^0$  and  $C^1$  elements for solving the Cahn-Hilliard equation. *Journal of Computational Physics*, 236:74 – 80, 2013.
- [55] J. Zhu, L.-Q. Chen, J. Shen, and V. Tikare. Coarsening kinetics from a variable-mobility Cahn-Hilliard equation: Application of a semi-implicit Fourier spectral method. *Phys. Rev. E*, 60:3564–3572, Oct 1999.